

Lawrence Berkeley National Laboratory

Lawrence Berkeley National Laboratory

Title

GAS-PARTICLE FLOW IN THE ENTRY REGION OF A CURVED PIPE

Permalink

<https://escholarship.org/uc/item/11m8b96t>

Author

Yeung, Woon-Shing

Publication Date

1979-04-01



Lawrence Berkeley Laboratory

UNIVERSITY OF CALIFORNIA

Materials & Molecular Research Division

GAS-PARTICLE FLOW IN THE ENTRY REGION OF A CURVED PIPE

Woon-Shing Yeung
(Ph. D. thesis)

April 1979

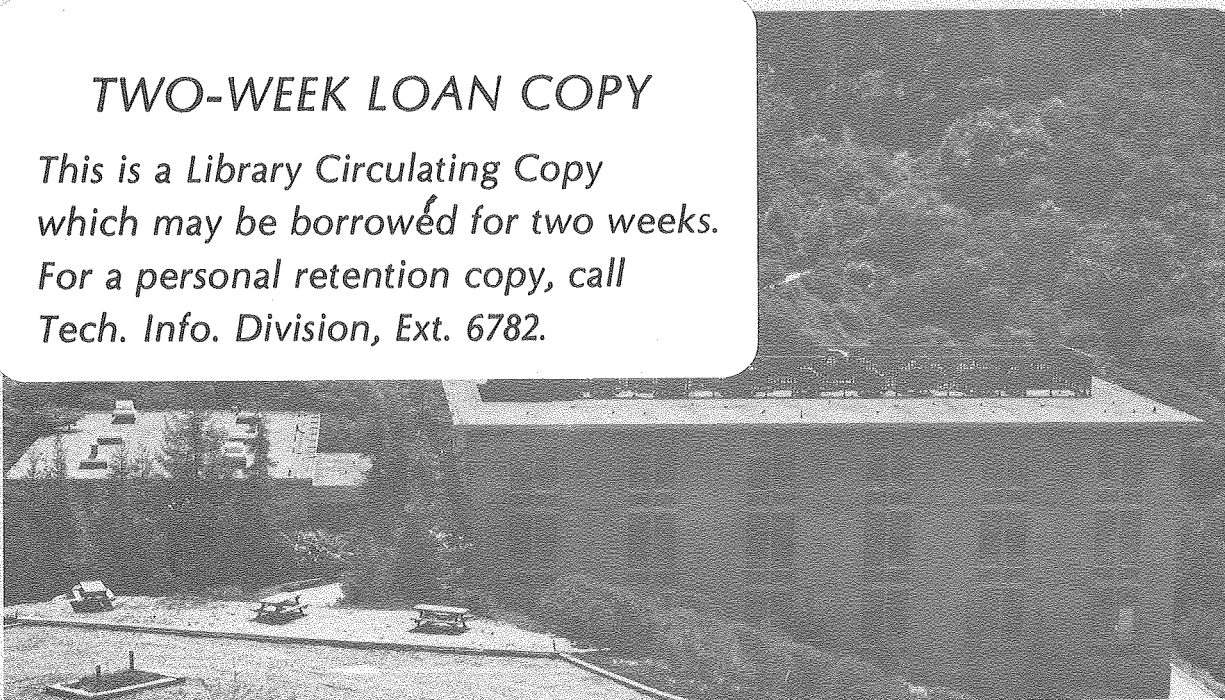
RECEIVED
LAWRENCE
BERKELEY LABORATORY

NOV 16 1979

LIBRARY AND
DOCUMENTS SECTION

TWO-WEEK LOAN COPY

*This is a Library Circulating Copy
which may be borrowed for two weeks.
For a personal retention copy, call
Tech. Info. Division, Ext. 6782.*



LBL-9905 c.2

DISCLAIMER

This document was prepared as an account of work sponsored by the United States Government. While this document is believed to contain correct information, neither the United States Government nor any agency thereof, nor the Regents of the University of California, nor any of their employees, makes any warranty, express or implied, or assumes any legal responsibility for the accuracy, completeness, or usefulness of any information, apparatus, product, or process disclosed, or represents that its use would not infringe privately owned rights. Reference herein to any specific commercial product, process, or service by its trade name, trademark, manufacturer, or otherwise, does not necessarily constitute or imply its endorsement, recommendation, or favoring by the United States Government or any agency thereof, or the Regents of the University of California. The views and opinions of authors expressed herein do not necessarily state or reflect those of the United States Government or any agency thereof or the Regents of the University of California.

Gas-Particle Flow in the Entry Region of a Curved Pipe

By

Woon-Shing Yeung

ABSTRACT

The flow of a dilute gas-particle mixture entering a circular curved pipe has been investigated. The fluid is assumed to be incompressible and the flow nonseparating and laminar. Individual numerical schemes have been devised to handle the two different regions of the fluid flow field, i.e., the irrotational core region and viscous boundary layer region. Thus, in the core region, the traditional Telenin's method is modified to obtain a numerical solution for the velocity potential function. For the viscous boundary layer, the orthonormal version of the method of integral relations is applied together with a backward difference scheme for the cross derivative terms. Interaction between the two regions is also accounted for by means of a simple iteration scheme. Final results are then presented and comparisons with other theoretical and experimental results are made whenever appropriate. Since we have assumed an irrotational core, the uniform entry profile changes to a two-dimensional potential vortex shortly downstream of the entry section. This is consistent with a recent experimental investigation on entry curved pipe flow by Agrawal, Talbot and Gong. There is also a cross flow directed from the outer bend towards the inner bend in the immediate neighborhood of the entry section. Further downstream, the cross flow reverses its direction and moves from the inner bend towards

the outer bend, as is generally reported in all curved pipe investigations. The axial profile, however, does not change drastically from that of a uniform profile because of the weak interaction between the core and boundary layer region for the values of Reynolds number considered in this report ($10^4 \sim 10^5$).

The remainder of the report discusses the dynamics of the particle phase. Lagrangian equations of motion for the particle phase are used. Due to the complexity of the momentum coupling between the two phases (i.e., the gas phase and the particle phase), only the first order solution for the particle phase has been obtained by neglecting its effect on the gas flow field. This has been proved adequate, for example in the erosion calculation of a curved pipe carrying a gas-solid mixture. Asymptotic expansion solutions for the particle trajectories are discussed. Finally, the density of the particle at the pipe wall is presented and discussion based on the numerical results are made.

ACKNOWLEDGMENT

I am particularly indebted to Professor M. Holt for his constant guidance and advice during my entire stay at Berkeley. Without his efforts, my experience here would never have been so pleasant and smooth.

Special thanks are due to Alan Levy for his encouragement and continued funding during the course of the research; to Professor S. A. Berger for his valuable comments and suggestions on the material in this manuscript; to Dr. J. J. Chattot for his useful discussions on the numerical schemes; to Sheila Slavin for her immense skill in typing this manuscript; and to all my friends who have reminded me once in a while that there is more to life than just study.

Finally, I would like to express my deepest gratitude to the important people in my life. To my wife, Donna, who has shared my life ever since I began my graduate studies here. Her contribution to my achievement as a loving and caring wife is as important as my own. To my parents, my brother Tak-Chiu, my sisters, Kit-Yuk and Kit-Wah, who have all given me the opportunity to pursue higher studies and to achieve the goal I have always dreamed of: the doctorate degree. To my family, then, I sincerely dedicate this thesis.

This work was supported by the U. S. Department of Energy under Contract W-7405-ENG-48.

TABLE OF CONTENTS

	<u>Page</u>
List of Figures	iii
List of Symbols	v
Chapter I Introduction	1
Chapter II Flow of a Gas Into a Curved Pipe	3
2.0 Historical Development	3
2.1 Equations of Motion	6
2.2 Flow Outside the Boundary Layer	8
2.3 Flow Inside the Boundary Layer	27
2.4 Results and Discussion for the Entry Curved Pipe Flow	45
Chapter III Particle Phase	50
3.0 Some Fundamentals of the Particulate Phase in a Gas Solid Mixture	50
3.1 Equations of Motion for the Two Phase System	52
3.2 Particle Trajectories and Density Distribution Along the Pipe Wall	57
3.3 Results and Discussion	60
Chapter IV Conclusions	63
References	65
Figures	68
Appendix	89

LIST OF FIGURES

- Fig. 1 Toroidal coordinate system.
- Fig. 2 Grid system and nodal point coordinates in the core region.
- Fig. 3 Notation of the mesh size in the streamwise direction in the core region.
- Fig. 4 Comparison of numerical solution by the modified Telenin's method to the exact analytical solution of the Laplace equation in a circular cylinder.
- Fig. 5 Contour of the potential function Ω in a curved pipe with $\alpha = 0.1$: (a) $s_o = (0.1)(\frac{\pi}{2})$, (b) $s_o = (0.4)(\frac{\pi}{2})$
Boundary conditions $f_1 = f_2 = 1 + \alpha r_o \cos \psi_o$, $f_3 = 0$.
- Fig. 6 Variation of Ω along the pipe.
- Fig. 7 Cross flow in a curved pipe with $\alpha = 0.1$: (a) $s_o = 0$,
(b) $s_o = (0.1) \frac{\pi}{2}$.
- Fig. 8 Axial velocity profile at plane of symmetry at
(a) $s_o = (0.1) \frac{\pi}{2}$, (b) $s_o = (0.2)(\frac{\pi}{2})$.
- Fig. 9 Displacement thickness along the pipe.
- Fig. 10 Variation of displacement thickness with azimuthal angle ψ .
- Fig. 11 Average nondimensional velocity in the boundary layer along the pipe.
- Fig. 12 Variation of \bar{V} with ψ at different streamwise stations.
- Fig. 13 Velocity profiles across the boundary layer.
- Fig. 14 Cross flow in the core region: (a) $\tilde{s} = 0.05$, (b) $\tilde{s} = 0.1$,
(c) $\tilde{s} = 0.2$, (d) $\tilde{s} = 0.4$, (e) $\tilde{s} = 0.5$, (f) $\tilde{s} = 0.6$.
- Fig. 15 Axial velocity profile in the core region: (a) $\tilde{s} = 0.05$,
(b) $\tilde{s} = 0.1$, (c) $\tilde{s} = 0.2$, (d) $\tilde{s} = 0.3$, (e) $\tilde{s} = 0.5$, (f) Legend.

- Fig. 16 Cylindrical polar coordinate and corresponding velocity components.
- Fig. 17 Schematic representation of the stream tube and other related notations.
- Fig. 18 Particle trajectories for various \tilde{L}_m in a curved pipe with $\alpha = 0.1$.
- Fig. 19 (a) Area of outer bend intercepted by particles; (b) initial grid size for the particle phase.
- Fig. 20 Density distribution of particle at the pipe wall for two values of \tilde{L}_m .
- Fig. 21 Variation of impingement velocity, impingement angle and density distribution along the first impact points, with $\alpha = 0.1$, $\tilde{L}_m = 0.5$ and $\bar{z}_0 = 0.1$.

LIST OF SYMBOLS

Capital Letters

A_{ij}	Coefficient matrix for the Lagrangian approximation in Eq. (2.2.41).
\underline{A}	Coefficient matrix of system (2.2.54).
B_{ij}	Coefficient matrix for the cosine approximation in Eq. (2.2.47).
C	Parameter in the axial velocity profile.
C^1_{ij}	Coefficient matrix for $\partial/\partial r_0$ derivative.
C^2_{ij}	Coefficient matrix for $\partial/\partial \psi_0$ derivative.
\underline{C}	Column vector containing the right-hand side of (2.2.54).
$C(k), k=1, \dots, N$	Right-hand side of (2.3.12).
D^1_{ij}	Coefficient matrix for $\partial^2/\partial r_0^2$ derivative.
D^2_{ij}	Coefficient matrix for $\partial^2/\partial \psi_0^2$ derivative.
D	Dean number $Re \sqrt{\alpha}$.
$D(k), k=1, \dots, N$	Right-hand side of (2.3.14).
I	Identity matrix.
J_{ik}	Given by $(1 + \alpha r_{0,i} \cos \psi_{0,k})$.
\tilde{L}_m	Nondimensional momentum equilibration length $\frac{W_i \tau_m}{R}$.
M_0	Particle flow rate at the initial plane.
N	Order of M.I.R.
$NX1$	Number of intervals in radial direction.
$NX2$	Number of intervals in azimuthal direction.
$NX3$	Number of intervals in streamwise direction.

P	Nondimensional pressure in boundary layer.
P_o	Nondimensional pressure in core region.
R	Mean radius of curvature of curved pipe.
Re	Reynolds number $W_i a / \nu$.
S	Azimuthal velocity gradient $\partial V / \partial \psi$.
(U, V, W)	Nondimensional velocity components inside the boundary layer.
(U_o, V_o, W_o)	Nondimensional velocity components in core region.
W_i	Entry velocity.
\tilde{X}	Column vector of the unknown potential at each node.
(X, Y, Z)	Cartesian coordinate system.
Z	Reciprocal of streamwise shear stress $(\partial W / \partial \eta)^{-1}$.
\tilde{Z}	Modified inverse shear stress $(\partial W / \partial \tilde{\eta})^{-1}$.

Small Letters

a	Radius of pipe.
a_{kj}	Coefficient for the orthonormal functions $\{g_k\}$.
$\{b_{k1}, k = 0, \dots, N-1\}$	Coefficients in the representation of Z .
$\{b_{k2}, k = 1, \dots, N\}$	Coefficients in the representation of V .
c_{kj}	Coefficient for the orthonormal functions $\{h_k\}$.
$\{e_j, j = 1, \dots, N\}$	Coefficients in the representation of S .
f_1	Entry condition.
f_2	Exit condition.
g	Exit condition.
$\{g_k\}$	Orthonormal function set $\int_0^1 g_i g_j \frac{1-W}{W} dW = \delta_{ij}$.
$\{h_k\}$	Orthonormal function set $\int_0^1 h_i h_j W^2 dW = \delta_{ij}$.
h	Step size in the streamwise direction.
(h_1, h_2, h_3)	Scale factor for the toroidal coordinate.

p	Pressure.
(r, ψ, ϕ)	Toroidal coordinate system.
(r_o, ψ_o, s_o)	Nondimensional coordinate.
(\bar{r}, \bar{z}, ϕ)	Nondimensional cylindrical coordinate.
s	Streamwise variable ϕ/α .
\tilde{s}	Modified streamwise variable $\phi/\pi/2$.
\bar{t}	Lagrangian variable in the particle equation of motion.
(u, v, w)	Velocity components.

Greek Letters

α	Radius ration a/R .
β	Density ratio ρ_p/ρ_f .
η	Boundary layer coordinate $\frac{a-r}{a} D^{\frac{1}{2}}$.
$\tilde{\eta}$	Boundary layer coordinate $\frac{a-r}{a} R_e^{\frac{1}{2}}$.
δ	Boundary layer thickness.
δ_1	Displacement thickness.
ω	Constant for the relaxation scheme.
τ_m	Momentum equilibration time.
ν	Kinematic viscosity
ρ	Density.
ζ	Blasius variable.
σ	Particle diameter.
Ω	Velocity potential in the core region.
Σ	Area element at the pipe surface.
$\vec{\nabla}$	Gradient operator.

Subscripts

e	Outer edge of boundary layer.
p	Particle phase.
f	Fluid phase.

I. INTRODUCTION

The study of two-phase flow systems has been a subject of wide interest owing to its broad applications to various physical problems. Recently, with the development of large coal gasification plants under the Energy Research and Development Administration (ERDA), it has become necessary to investigate the fluid dynamics of gas-particle flows, both experimentally and theoretically, in order to design better piping systems and vessels that handle such flows.

One of the most common components that is present in nearly all piping systems of a coal gasification plant is the elbow of circular cross-section. It is, therefore, the purpose of the present work to study the fluid mechanics of a gas-solid mixture flowing into a curved pipe from a large reservoir, such as a coal gasifier. Results from such analyses should enable us to predict, in particular, the erosion characteristics inside the bend due to the impact of the solid particles with the pipe wall.

Historically, gas-particle flow analyses have had a wide application to various fields of importance, such as rocket nozzle performance analyses, aerosol studies, pneumatic conveying systems, etc. The majority of the earlier work has been limited to simple flow geometries. Kliegel (1963), Rudinger (1970) and Gilbert, Allport and Dunlap (1962) considered the one-dimensional gas-particle flow inside a rocket nozzle. Soo (1965, 1968) investigated both the laminar and separated flow of a particulate suspension for various systems. Pipe flow of a dilute suspension was extensively studied by Soo and Tung (1971,1972), who took into account the effects of deposition, entrainment, gravity and electrostatic force in their analyses. The compressible boundary layer of a gas-particle

flow over a flat plate was treated by Singleton (1965).

Little work has been done for more complicated systems. One major difficulty is to obtain analytical, whenever possible, or numerical solutions of the fluid phase alone. Without such solutions, one cannot hope to obtain solutions for the particulate phase. This explains why the earlier work mentioned before was mainly confined to simple geometries in which the dynamics of the fluid phase can be solved quite easily. In the present case of a curved pipe geometry, the situation is more complicated because of the three dimensionality of the problem. As a result, the present work is restricted to a dilute suspension so that the gas flow field is negligibly affected by the presence of the particles. In this respect, the gas flow field can be solved independently of the particle phase.

This report is divided into two main parts. The first part discusses in detail the full numerical solution for the problem of a pure fluid entering a curved pipe of circular cross-section. The flow is assumed to be steady, laminar and incompressible. Instead of solving the full three-dimensional Navier Stokes equations, the classical approach of dividing the gas flow field into an inviscid and viscous region is followed. Individual numerical solutions for both regions are sought. Finally, their interaction through the displacement thickness is included in the analysis. Comparison of other analytical and experimental results are also made here.

The second part contains a discussion of the fundamental behavior of the particulate phase in a gas-solid mixture. The particle motion is then solved using a simple Lagrangian analysis. Discussion will be made based on the present numerical results. Circumstances under which exact solution of the particle trajectories is possible are also discussed.

II. FLOW OF A GAS INTO A CURVED PIPE

2.0 Historical development

When a fluid flows through a curved pipe, a pressure gradient directed towards the center of curvature is developed to balance the centrifugal force exerted on individual fluid elements. Because of viscosity, the fluid near the wall moves more slowly than the fluid away from the wall and consequently requires a smaller pressure gradient to balance the centrifugal force. The differences in these pressure gradients creates a secondary flow inside the boundary layer in which the fluid moves from the outer bend towards the inner bend of the pipe.

The first theoretical studies of fully developed curved pipe flow were made by Dean (1927,1928). He showed that the appropriate dynamical similarity parameter is the Dean number, defined as $Re(a/R)^{\frac{1}{2}}$, where Re is the Reynolds number based on the mean flow velocity and the radius of the circular cross-section, a ; and R is the mean radius of curvature of the pipe. Since then, a number of numerical investigations were made in this area, particularly those of McConalogue and Sirvastava (1968), Collins and Dennis (1975) and Greenspan (1973). These authors considered the full Navier-Stokes equations in the fully developed region and their schemes suffered a serious drawback at high Reynolds number. Later, Smith (1976a) investigated the steady curved pipe flow with general cross-section. He pointed out that laminar attached flow through a curved pipe with a rectangular cross-section does not exist. On the other hand, asymptotic boundary layer theories for large values of Dean number were studied, first by Baura (1963) and later by Ito (1969). The unsteady fully developed curved pipe flow subjected to a pulsatile pressure gradient

was investigated by Lyne (1970).

Comparatively little literature deals with the entry flow in a curved pipe owing to the complicated nature of the problem. Earlier analyses were mainly made using an inviscid rotational model developed by Hawthorne (1953). The first complete analyses of a viscous fluid flowing into a curved pipe were, to the author's knowledge, those of Yao and Berger (1974) and Singh (1974). Special assumptions regarding the inviscid core were made in Yao et al.'s analysis. Smith (1976b) considered the case of a fluid flowing into a curved pipe from a straight section. Perturbation methods were used in Singh's and Smith's work which render their solution valid only for a small distance from the entry section. Most recently, Agrawal, Talbot and Gong (1978) have measured experimentally the velocity profiles in the entry region of a curved pipe. They find that the initially uniform velocity profile changes to a potential vortex profile immediately downstream of the entry section. At the same time, Choi (1978) investigated the unsteady entry flow in a curved tube experimentally. These experimental results were only for moderate values of Dean number.

In the present study, full numerical schemes are proposed to solve the entry flow problem at very large Dean number. The physical situation corresponds to a gas leaving a large reservoir and entering a curved pipe with circular cross section. There are existing finite difference schemes aiming at solving the three-dimensional Navier-Stokes equations. However, almost all are restricted to low and moderate values of Reynolds number. It is thus practical to use boundary layer theory for the present problem. The boundary layer is assumed to be laminar and attached throughout the whole analysis. Where the boundary layer becomes separated or turbulent (a rough estimate can be made of the transition to turbulent boundary

layer by using the flat plate result, i.e., when the Reynolds number based on the distance from the entry location is of the order of 10^5), the present results will not be valid. For the inviscid core region, it is further assumed that the flow is irrotational.

2.1 Equations of Motion

It is convenient to use a set of toroidal coordinates (r, ψ, ϕ) as shown in Fig. 1. Denote by R the radius of curvature of the pipe axis, by a the radius of the cross-section and by u, v, w the velocity components in the direction of increasing r, ψ and ϕ , respectively. The equations of transformation from the Cartesian coordinates (X, Y, Z) to the present toroidal coordinates are

$$\begin{aligned} X &= (R + r \cos \psi) \cos \phi, \\ Y &= r \sin \psi, \\ Z &= (R + r \cos \psi) \sin \phi. \end{aligned} \quad (2.1.1)$$

The corresponding scale factors for the toroidal coordinates system are then given by

$$h_1 = 1, \quad h_2 = r, \quad h_3 = R + r \cos \psi. \quad (2.1.2)$$

With the help of (2.1.2), the familiar Navier-Stokes equations can be written, in component forms, as follows: for the r -momentum

$$\begin{aligned} u \frac{\partial u}{\partial r} + \frac{v}{r} \frac{\partial u}{\partial \psi} + \frac{w}{R + r \cos \psi} \frac{\partial u}{\partial \phi} - \frac{v^2}{r} - \frac{w^2 \cos \psi}{R + r \cos \psi} \\ = -\frac{1}{\rho} \frac{\partial p}{\partial r} + \nu \left\{ \frac{1}{(R + r \cos \psi)^2} \frac{\partial}{\partial \phi} \left[\frac{\partial u}{\partial \phi} - w \cos \psi - (R + r \cos \psi) \frac{\partial w}{\partial r} \right] \right. \\ \left. - \left(\frac{1}{r} \frac{\partial}{\partial \psi} - \frac{\sin \psi}{R + r \cos \psi} \right) \left(\frac{\partial v}{\partial r} + \frac{v}{r} - \frac{1}{r} \frac{\partial u}{\partial \psi} \right) \right\}, \end{aligned} \quad (2.1.3)$$

for the ψ -momentum

$$\begin{aligned} u \frac{\partial v}{\partial r} + \frac{v}{r} \frac{\partial v}{\partial \psi} + \frac{w}{R + r \cos \psi} \frac{\partial v}{\partial \phi} + \frac{uv}{r} + \frac{w^2 \sin \psi}{R + r \cos \psi} \\ = -\frac{1}{r\rho} \frac{\partial p}{\partial \psi} + \nu \left\{ \left(\frac{\partial}{\partial r} + \frac{\cos \psi}{R + r \cos \psi} \right) \left(\frac{\partial v}{\partial r} + \frac{v}{r} - \frac{1}{r} \frac{\partial u}{\partial \psi} \right) \right. \\ \left. - \frac{1}{(R + r \cos \psi)^2} \frac{\partial}{\partial \phi} \left[\frac{R + r \cos \psi}{r} \frac{\partial w}{\partial \psi} - w \sin \psi - \frac{\partial v}{\partial \phi} \right] \right\}, \end{aligned} \quad (2.1.4)$$

and for the ϕ momentum

$$\begin{aligned}
 u \frac{\partial w}{\partial r} + \frac{v}{r} \frac{\partial w}{\partial \psi} + \frac{w}{R+r \cos \psi} \frac{\partial w}{\partial \phi} + \frac{uw \cos \psi}{R+r \cos \psi} - \frac{vw \sin \psi}{R+r \cos \psi} \\
 = - \frac{1}{R+r \cos \psi} \frac{1}{\rho} \frac{\partial p}{\partial \phi} + v \left\{ \left(\frac{\partial}{\partial r} + \frac{1}{r} \right) \left[\frac{\partial w}{\partial r} - \frac{1}{R+r \cos \psi} \left(\frac{\partial u}{\partial \phi} - w \cos \psi \right) \right] \right. \\
 \left. + \frac{1}{r} \frac{\partial}{\partial \psi} \left[\frac{1}{r} \frac{\partial w}{\partial \psi} - \frac{1}{R+r \cos \psi} \left(\frac{\partial v}{\partial \phi} + w \sin \psi \right) \right] \right\} . \quad (2.1.5)
 \end{aligned}$$

The continuity equation is

$$\frac{\partial(ur)}{\partial r} + \frac{\partial v}{\partial \psi} + \frac{r}{R+r \cos \psi} \frac{\partial w}{\partial \phi} + \frac{ur \cos \psi - vr \sin \psi}{R+r \cos \psi} = 0 . \quad (2.1.6)$$

The domain of interest is

$$0 < r < 1 , \quad 0 < \psi < \pi , \quad 0 < \phi < \pi/2 . \quad (2.1.7)$$

The planes $\psi = 0$ and $\psi = \pi$ are planes of symmetry and it is thus adequate to consider only the top half of the flow field. The necessary boundary conditions are

- (i) no slip condition $u = v = w = 0$ at $r = a$
 - (ii) uniform entry $w = W_i = \text{constant}$ at $\phi = 0$
 - (iii) exit conditions given at $\phi = \pi/2$.
- (2.1.8)

Most authors impose fully developed conditions at the exit of the pipe. However, this may not be true for flow into a 90° elbow at high Reynolds number. Moreover, the amount of information required at $\phi = \pi/2$ depends also on the method of solution for the Navier-Stokes equation. Hence, we only specify for the moment that some exit conditions are given and clarify these conditions whenever appropriate.

2.2 Flow outside the boundary layer

Since the viscous effect is essentially confined to the boundary layer, the core region is assumed to be inviscid. The governing equations are, therefore, the Euler equations, which can be obtained from the Navier-Stokes equations by neglecting the viscous terms. Using the following variables

$$\begin{aligned} U_o &= \frac{u}{W_i} , \quad V_o = \frac{v}{W_i} , \quad W_o = \frac{w}{W_i} , \quad P_o = \frac{p}{\rho W_i^2} , \\ r_o &= \frac{r}{a} , \quad \psi_o = \psi , \quad s_o = \phi , \end{aligned} \quad (2.2.1)$$

and define the radius ratio, α , to be

$$\alpha = \frac{a}{R}$$

we can write the Euler equations as follows:

$$U_o \frac{\partial U_o}{\partial r_o} + \frac{V_o}{r_o} \frac{\partial U_o}{\partial \psi_o} + \frac{\alpha W_o}{1 + \alpha r_o \cos \psi_o} \frac{\partial U_o}{\partial s_o} - \frac{V_o^2}{r_o} - \frac{\alpha W_o^2 \cos \psi_o}{1 + \alpha r_o \cos \psi_o} = - \frac{\partial P_o}{\partial r_o} , \quad (2.2.2)$$

$$U_o \frac{\partial V_o}{\partial r_o} + \frac{V_o}{r_o} \frac{\alpha W_o}{1 + \alpha r_o \cos \psi_o} \frac{\partial V_o}{\partial s_o} + \frac{U_o V_o}{r_o} + \frac{\alpha W_o^2 \sin \psi_o}{1 + \alpha r_o \cos \psi_o} = - \frac{1}{r_o} \frac{\partial P_o}{\partial \psi_o} , \quad (2.2.3)$$

$$U_o \frac{\partial W_o}{\partial r_o} + \frac{V_o}{r_o} \frac{\partial W_o}{\partial \psi_o} + \frac{\alpha W_o}{1 + \alpha r_o \cos \psi_o} \frac{\partial W_o}{\partial s_o} + \frac{\alpha U_o W_o \cos \psi_o - \alpha V_o W_o \sin \psi_o}{1 + \alpha r_o \cos \psi_o} = - \frac{\alpha}{1 + \alpha r_o \cos \psi_o} \frac{\partial P_o}{\partial s_o} . \quad (2.2.4)$$

The continuity equation becomes

$$\frac{\partial(U_o r_o)}{\partial r_o} + \frac{\partial V_o}{\partial \psi_o} + \frac{\alpha r_o}{1 + \alpha r_o \cos \psi_o} \frac{\partial W_o}{\partial s_o} + \frac{\alpha(U_o \cos \psi_o - V_o \sin \psi_o)}{1 + \alpha r_o \cos \psi_o} = 0 . \quad (2.2.5)$$

Given enough boundary conditions on the entry plane, the exit plane and the pipe wall, one can solve equations (2.2.2) to (2.2.5) for U_o, V_o, W_o and P_o numerically. However, the nonlinearity and three-dimensional nature of the Euler equations present great difficulties in constructing

efficient and economical numerical schemes. In view of this, we shall further assume that the core region be irrotational. This greatly simplifies the present problem because we can define a potential function Ω such that

$$U_o = \frac{1}{\alpha} \frac{\partial \Omega}{\partial r_o} , \quad V_o = \frac{1}{\alpha r_o} \frac{\partial \Omega}{\partial \psi_o} , \quad W_o = \frac{1}{1 + \alpha r_o \cos \psi_o} \frac{\partial \Omega}{\partial s_o} . \quad (2.2.6)$$

Substitute (2.2.6) into the continuity equation (2.2.5) and obtain the standard Laplace equation in the toroidal coordinates:

$$\begin{aligned} \frac{\partial^2 \Omega}{\partial r_o^2} + \frac{\partial \Omega}{\partial r_o} \left[\frac{1}{r_o} + \frac{\alpha \cos \psi_o}{1 + \alpha r_o \cos \psi_o} \right] + \frac{1}{r_o^2} \frac{\partial^2 \Omega}{\partial \psi_o^2} - \frac{\alpha \sin \psi_o}{1 + \alpha r_o \cos \psi_o} \frac{\partial \Omega}{\partial \psi_o} \\ + \frac{\alpha^2}{(1 + \alpha r_o \cos \psi_o)^2} \frac{\partial^2 \Omega}{\partial s_o^2} = 0 . \end{aligned} \quad (2.2.7)$$

Equation (2.2.7) is to be solved subject to the following Neumann conditions:

$$\begin{aligned} \frac{\partial \Omega}{\partial s_o} &= f_1(r_o, \psi_o) \quad \text{at} \quad s_o = 0 , \\ \frac{\partial \Omega}{\partial s_o} &= f_2(r_o, \psi_o) \quad \text{at} \quad s_o = \pi/2 , \\ \frac{\partial \Omega}{\partial r_o} &= f_3(\psi_o, s_o) \quad \text{at} \quad r_o = 1 , \end{aligned} \quad (2.2.8)$$

where f_1, f_2 and f_3 are prescribed functions of the indicated variables. Although the above formulation is general, it should be mentioned that, in the present studies, we limit ourselves to certain classes of functions for Ω and for the boundary conditions. In particular, Ω is an even function in ψ_o and so are the boundary conditions.

The assumption of irrotationality may seem drastic. Nevertheless, it avoids the difficult Euler equations and also provides some fundamental insights, both analytically and numerically, as we shall see in the following sections.

Approximate solution of Laplace equation

Before discussing the full numerical scheme for solving equation (2.2.7) subject to (2.2.8), let us consider the case when α is small ($\alpha < 1$ in all curved pipes of circular cross section). We take the boundary conditions as:

$$f_1 = 1 + \alpha r_o \cos \psi_o, \quad f_2 = 1 + \alpha r_o \cos \psi_o, \quad f_3 = 0. \quad (2.2.9)$$

(2.2.9) corresponds to the uniform entry and exit conditions with zero normal velocity at the pipe wall. Following the method of matched asymptotic expansion (Van Dyke, 1964) with α being the small parameter, we assume Ω , the outer solution, to be expanded in a power series in α :

$$\Omega = \Omega_o + \alpha \Omega_1 + \alpha^2 \Omega_2 + \dots \quad (2.2.10)$$

Substituting (2.2.10) into (2.2.7), we have, for $O(1)$

$$\frac{\partial^2 \Omega_o}{\partial r_o^2} + \frac{1}{r_o} \frac{\partial \Omega_o}{\partial r_o} + \frac{1}{r_o^2} \frac{\partial^2 \Omega_o}{\partial \psi_o^2} = 0, \quad \left. \frac{\partial \Omega_o}{\partial r_o} \right|_{r_o=1} = 0 \quad (2.2.11)$$

The solution is

$$\Omega_o = g_o(s_o), \quad (2.2.12)$$

where $g_o(s_o)$ is a function of s_o only.

For $O(\alpha)$, we have

$$\frac{\partial^2 \Omega_1}{\partial r_o^2} + \frac{1}{r_o} \frac{\partial \Omega_1}{\partial r_o} + \frac{1}{r_o^2} \frac{\partial^2 \Omega_1}{\partial \psi_o^2} = 0, \quad \left. \frac{\partial \Omega_1}{\partial r_o} \right|_{r_o=1} = 0 \quad (2.2.13)$$

with corresponding solution

$$\Omega_1 = g_1(s_o), \quad (2.2.14)$$

where $g_1(s_o)$ is also a function of s_o only.

Clearly the above solution is not valid near the entry and the exit planes. To obtain the inner solution near the entry plane, we scale the dependent variable and s_o as follows

$$\tilde{\Omega} = \frac{\Omega}{\alpha} \quad , \quad s_o^* = \frac{s_o}{\alpha} \quad . \quad (2.2.15)$$

$\tilde{\Omega}$ and s_o^* are known as the inner variables. Again, we express $\tilde{\Omega}$ as

$$\tilde{\Omega} = \tilde{\Omega}_0 + \alpha \tilde{\Omega}_1 + \dots \quad (2.2.16)$$

The first order inner problem is given by

$$\begin{aligned} \frac{\partial^2 \tilde{\Omega}_0}{\partial r_o^2} + \frac{1}{r_o} \frac{\partial^2 \tilde{\Omega}_0}{\partial r_o} + \frac{1}{r_o^2} \frac{\partial^2 \tilde{\Omega}_0}{\partial \psi_o^2} + \frac{\partial^2 \tilde{\Omega}_0}{\partial s_o^{*2}} = 0 \quad , \\ \left. \frac{\partial \tilde{\Omega}_0}{\partial r_o} \right|_{r_o=1} = 0 \quad , \quad \left. \frac{\partial \tilde{\Omega}_0}{\partial s_o^*} \right|_{s_o^*=0} = 1 \quad , \quad \tilde{\Omega}_0 \text{ bounded as } s_o^* \rightarrow \infty \quad . \end{aligned} \quad (2.2.17)$$

Using separation of variables, $\tilde{\Omega}_0$ is found to be

$$\tilde{\Omega}_0 = \sum_{m=1}^{\infty} \sum_{n=1}^{\infty} A_{nm}^+ J_m(\beta_{nm} r_o) \cos m \psi_o e^{-\beta_{nm} s_o^*} \quad , \quad (2.2.18)$$

where $\beta_{1m}, \beta_{2m}, \dots$ etc. are roots of the equation

$$J'_m(\beta_{nm}) = 0 \quad .$$

The condition $m > 1$ insures the roots $\beta_{nm} > 0$ for all n and m . This is required because if $\beta_{nm} = 0$ for some n and m , the inner solution will converge to a function of r_o and ψ_o as $s_o^* \rightarrow \infty$. This is incompatible with the outer solution, which depends only on s_o . A_{nm}^+ are found formally from the condition at $s_o^* = 0$,

$$A_{nm}^+ = \frac{-\beta_{nm} \int_0^1 \int_0^\pi J_m(\beta_{nm} r_o) \cos m \psi_o r_o dr_o d\psi_o}{\int_0^1 \int_0^\pi J_m^2(\beta_{nm} r_o) \cos^2 m \psi_o r_o dr_o d\psi_o} \quad . \quad (2.2.19)$$

In view of (2.2.15), the inner solution is actually of order α relative to the $O(1)$ outer solution, Ω_o . Thus, we may write to order α^2 , the outer and inner solutions as follows:

Outer solution:

$$\Omega^{(o)} = g_o(s_o) + \alpha g_1(s_1) + O(\alpha^2) \quad . \quad (2.2.20)$$

Inner solution:

$$\Omega_+^{(i)} = \alpha \tilde{\Omega}_o + O(\alpha^2) \quad , \quad (2.2.21)$$

where $\Omega^{(o)}$ denotes the outer solution and $\Omega_+^{(i)}$ denotes the inner solution near the entry plane. Since the inner solution tends to zero as $s_o^* \rightarrow \infty$, we must have, for the outer solution, at $s_o = 0$

$$g_o(0) = 0 \quad , \quad g_1(0) = 0 \quad . \quad (2.2.22)$$

In order to find the functional form of g_o and g_1 , one must apply the global mass conservation law, which simply requires that the mass flow rate at any s_o must be constant, or

$$\int_0^\pi \int_0^1 W_o r_o dr_o d\psi_o = C_1 \quad , \quad (2.2.23)$$

or

$$\int_0^\pi \int_0^1 \frac{1}{1 + \alpha r_o \cos \psi_o} \frac{\partial \Omega}{\partial s_o} r_o dr_o d\psi_o = C_1 \quad ,$$

where C_1 is a constant given simply by the mass flow rate at the entry plane, $s_o = 0$:

$$C_1 = \int_0^\pi \int_0^1 r_o dr_o d\psi_o = \frac{\pi}{2} \quad . \quad (2.2.24)$$

Substituting equation (2.2.20) into (2.2.23) and using (2.2.22), we obtain, to order α ,

$$g_o(s_o) + \alpha g_1(s_1) = C_2 s_o$$

where C_2 is given by

$$C_2 = C_1 / \int_0^\pi \int_0^1 \frac{r_o dr_o d\psi_o}{1 + \alpha r_o \cos \psi_o} . \quad (2.2.25)$$

It follows then

$$g_o(s_o) = C_2 s_o \quad (2.2.26)$$

and

$$g_1(s_o) = 0 . \quad (2.2.27)$$

For the exit region, we redefine the outer variable as

$$\bar{s}_o = \frac{\pi}{2} - s_o . \quad (2.2.28)$$

The corresponding inner variable near the exit region is then

$$\bar{s}_o^* = \frac{\bar{s}_o}{\alpha} . \quad (2.2.29)$$

In view of (2.2.26), the first order inner solution must approach $C_2 \cdot \pi/2$ as the inner variable $\bar{s}_o^* \rightarrow \infty$. This suggests that no stretching is required for Ω in the exit region. Following the same procedure as described before, the order 1 inner problem is given by:

$$\begin{aligned} \frac{\partial^2 \bar{\Omega}_o}{\partial r_o^2} + \frac{1}{r_o} \frac{\partial \bar{\Omega}_o}{\partial r_o} + \frac{1}{r_o^2} \frac{\partial^2 \bar{\Omega}_o}{\partial \psi_o^2} + \frac{\partial^2 \bar{\Omega}_o}{\partial \bar{s}_o^{*2}} = 0 , \\ \left. \frac{\partial \bar{\Omega}_o}{\partial r_o} \right|_{r_o=1} = 0 , \quad \left. \frac{\partial \bar{\Omega}_o}{\partial \bar{s}_o^*} \right|_{\bar{s}_o^*=0} = 0 , \quad \bar{\Omega}_o \text{ bounded as } \bar{s}_o^* \rightarrow \infty . \end{aligned} \quad (2.2.30)$$

The bounded solution satisfying (2.2.30) and which matches (2.2.26) is

$$\bar{\Omega}_o = C_2 \cdot \pi/2 . \quad (2.2.31)$$

In a similar fashion, the order α problem is given by

$$\frac{\partial^2 \Omega_1^-}{\partial r_o^2} + \frac{1}{r_o} \frac{\partial \Omega_1^-}{\partial r_o} + \frac{1}{r_o^2} \frac{\partial^2 \Omega_1^-}{\partial \psi_o^2} + \frac{\partial^2 \Omega_1^-}{\partial s_o^{*2}} = 0 \quad , \quad (2.2.32)$$

$$\left. \frac{\partial \Omega_1^-}{\partial r_o} \right|_{r_o=1} = 0 \quad , \quad \left. \frac{\partial \Omega_1^-}{\partial s_o^*} \right|_{s_o^*=0} = -1 \quad , \quad \Omega_1^- \text{ bounded as } s_o^* \rightarrow \infty$$

with solutions

$$\Omega_1^- = \sum_{m=1}^{\infty} \sum_{n=1}^{\infty} A_{nm}^- J_m(\beta_{nm} r_o) \cos m \psi_o e^{-\beta_{nm} s_o^*} \quad , \quad (2.2.33)$$

where β_{nm} again satisfies $J'_m(\beta_{nm}) = 0$ and $A_{nm}^- = -A_{nm}^+$. The inner solution in the exit region, $\Omega_-^{(i)}$, is then given by

$$\Omega_-^{(i)} = \Omega_o^- + \alpha \Omega_1^- + O(\alpha^2) \quad . \quad (2.2.34)$$

A composite solution which is valid for the whole region can be constructed from the two inner solutions and the outer solution. It is found as

$$\Omega(r_o, \psi_o, s_o) = c_2 s_o + \alpha \left\{ \sum_{m=1}^{\infty} \sum_{n=1}^{\infty} A_{nm}^+ J_m(\beta_{nm} r_o) \cos m \psi_o \left(e^{-\beta_{nm} \frac{s_o}{\alpha}} - e^{-\beta_{nm} \frac{\frac{\pi}{2} - s_o}{\alpha}} \right) \right\} + O(\alpha^2) \quad (2.2.35)$$

where the condition $A_{nm}^- = -A_{nm}^+$ has been used.

Higher order solutions can be found readily. Solution (2.2.35) shows that the core flow develops quite fast into the potential vortex[†] profile and persists downstream until the exit region where it is adjusted again to satisfy the imposed exit condition. The existence of a potential vortex away from the entry and exit sections is, of course, anticipated since we have assumed an irrotational core and zero normal velocity at the wall. It is also consistent with the experimental findings of Agrawal, Talbot and Gong (1978). In the actual case where a boundary

[†]A potential vortex in toroidal coordinates is given by $\Omega = \text{const. } s_o$.

layer exists, the potential vortex profile will be altered before the exit is approached due to the interaction with the boundary layer.

In summary, it has been shown that the assumption of potential flow outside the boundary layer to calculate the early development of the core flow in a curved pipe is a reasonable one. Furthermore, it admits exact analytical solutions when the boundary conditions are simple enough. For more general boundary conditions or when α is not small enough, the solutions must be found numerically.

Numerical solution

Here we shall describe in detail the numerical scheme used in the present studies to solve equation (2.2.7) subject to the Neumann boundary conditions given on the entire boundary. That the problem is well-posed is very well established mathematically. Extensive numerical calculations have been applied to the three-dimensional Laplace equation with complicated geometries. The most commonly used method is based on the use of finite difference scheme. While the formulation of finite difference methods is quite straightforward, it is not our intent to use such approaches. Instead, we shall study alternative techniques aimed at eliminating finite difference calculations in selected coordinate directions, in the hope of improving the efficiency of the numerical scheme. One such method is Telenin's method (Gilinskii, Telenin and Tinyakov, 1964). It has been applied to numerous inviscid flow calculations (see Holt, 1977) and proved very efficient. We shall now describe the basic idea of Telenin's method.

In order to eliminate finite difference calculations in selected

coordinate directions, the unknowns are represented by appropriate interpolating functions in these coordinate directions. Partial derivatives in these chosen coordinates can then be evaluated analytically and, as a result, the original governing equations contain only partial derivatives in the remaining direction (or directions). In practice, the maximum number of coordinates are chosen so that the resulting system consists of ordinary differential equations. As described, Telenin's method can be applied to partial differential equations of elliptic, mixed elliptic-hyperbolic, or parabolic type.

The principal advantage of Telenin's method over conventional finite difference schemes lies in the freedom of choosing the interpolating functions. Thus, when certain functional properties of the unknowns (such as oddness, evenness or periodicity) are known, one can easily choose appropriate functions that exhibit those properties, thereby improving the accuracy of the numerical results. Furthermore, some boundary conditions can be carefully incorporated into such chosen functions, thus eliminating the need to consider the boundary points separately, as is required in finite difference formulation.

In the following, we shall apply Telenin's method to equation (2.2.7). We shall approximate Ω analytically in the cross flow plane, i.e., in r_o and ψ_o directions. The grid system is shown in Fig. 2. Owing to the artificial singularity at $r_o = 0$ in using the toroidal coordinates, we exclude the center of the semi-circular region for numerical purposes. Let (i,k) represent the coordinates of the nodes, i.e., on the point (i,k) , $r_o = r_{o,i}$ and $\psi_o = \psi_{o,k}$. The functional value of any function $f(r_o, \psi_o, s_o)$ at the node (i,k) will be denoted by $f_{ik}(s_o)$. Note that f_{ik} is only a function of s_o .

On planes of constant ψ_o , $\psi_o = \psi_{o,k}$, we approximate Ω by a Lagrangian

polynomial in the r_o direction:

$$\Omega = \sum_{j=1}^{NX1+1} \Omega_j^o r_o^{j-1} , \quad (2.2.36)$$

where $NX1$ is the number of nodes in the r_o direction and Ω_j^o depends only on ψ_o and s_o . Normally, one can only fit a $(NX1-1)$ degree polynomial into $NX1$ points. However, due to the derivative boundary condition at $r_o=1$, one has an extra degree of freedom in fitting a polynomial through $NX1$ points, i.e., one can fit an $NX1$ degree polynomial through the $NX1$ points. Rewrite (2.2.36) as

$$\Omega = \sum_{j=1}^{NX1} \Omega_j^o r_o^{j-1} + \Omega_{NX1+1}^o r_o^{NX1} . \quad (2.2.37)$$

Applying the boundary condition at $r_o=1$ from equation (2.2.8), Ω_{NX1}^o can be related to $f_3(\psi_o, s_o)$ by the following:

$$\Omega_{NX1+1}^o(\psi_o, s_o) = \frac{1}{NX1} \{f_3(\psi_o, s_o) - \sum_{j=2}^{NX1} (j-1) \Omega_j^o(\psi_o, s_o)\} . \quad (2.2.38)$$

Substituting (2.2.38) into (2.2.37) and simplifying, we obtain

$$\bar{\Omega} = \Omega_i^o + \sum_{j=2}^{NX1} \Omega_j^o \{r_o^{j-1} - \frac{j-1}{NX1} r_o^{NX1}\} , \quad (2.2.39)$$

where $\bar{\Omega}$ is defined as

$$\bar{\Omega} = \Omega - \frac{f_3(\psi_o, s_o) r_o^{NX1}}{NX1} . \quad (2.2.40)$$

The interpolating coefficients $\Omega_1^o, \Omega_2^o, \dots$ can be solved in terms of the nodal values of $\bar{\Omega}$. Thus, if we apply (2.2.39) to the $NX1$ points in the r_o direction, we have

$$\bar{\Omega}_{ik} = \sum_{j=1}^{NX1} A_{ij} \Omega_j^o , \quad i = 1, 2, \dots, NX1 , \quad (2.2.41)$$

where A_{ij} is given by

$$A_{ij} = 1 \quad \text{when } j = 1$$

and

$$A_{ij} = r_{o,i}^{j-1} - \frac{(j-1)}{NX1} r_{o,i}^{NX1}, \quad \text{otherwise} \quad . \quad (2.2.42)$$

Solving (2.2.41), we obtain

$$\Omega_i^o = \sum_{j=1}^{NX1} A_{ij}^{-1} \bar{\Omega}_{jk} \quad , \quad i = 1, 2, \dots, NX1 \quad . \quad (2.2.43)$$

In a straightforward manner, the partial derivatives in the r_o direction are given by

$$\frac{\partial \bar{\Omega}_{ik}}{\partial r_o} = \sum_{j=1}^{NX1} C_{ij} \bar{\Omega}_{jk} \quad (2.2.44)$$

where

$$C_{ij} = \sum_{l=2}^{NX1} (l-1) A_{lj}^{-1} (r_{o,i}^{l-2} - r_{o,i}^{NX1-1})$$

and

$$\frac{\partial^2 \bar{\Omega}_{ik}}{\partial r_o^2} = \sum_{j=1}^{NX1} D_{ij} \bar{\Omega}_{jk} \quad (2.2.45)$$

where

$$D_{ij} = \sum_{l=2}^{NX1} (l-1) A_{lj}^{-1} [(l-2) r_{o,i}^{l-3} - (NX1-1) r_{o,i}^{NX1-2}] \quad .$$

Similarly, on contours of constant r_o , $r_o = r_{o,i}$, Ω is expressed in cosine series because of its symmetry property as follows:

$$\Omega = \sum_{j=1}^{NX2} \Omega_j^{oo} \cos(j-1)\psi_o \quad , \quad (2.2.46)$$

where $NX2$ is the number of modes in the ψ_o direction. As before, Ω_j^{oo} , which is now a function of r_o and s_o only, is a linear combination of the values of Ω on the $NX2$ points. If a matrix B is defined as

$$B_{kj} = \cos(j-1)\psi_{o,k} \quad , \quad k, j = 1, \dots, NX2 \quad , \quad (2.2.47)$$

it can be shown that the following holds:

$$\Omega_j^{oo} = \sum_{\ell=1}^{NX2} B_{j\ell}^{-1} \Omega_{i\ell} \quad , \quad j = 1, \dots, NX2 \quad , \quad (2.2.48)$$

$$\frac{\partial \Omega_{ik}}{\partial \psi_o} = \sum_{j=1}^{NX2} C_{kj}^2 \Omega_{ij}$$

(2.2.49)

where

$$C_{kj}^2 = - \sum_{\ell=2}^{NX2} (\ell-1) B_{\ell j}^{-1} \sin(\ell-1) \psi_{o,k} \quad ,$$

and

$$\frac{\partial^2 \Omega_{ik}}{\partial \psi_o^2} = \sum_{j=1}^{NX2} D_{kj}^2 \Omega_{ij}$$

(2.2.50)

where

$$D_{kj}^2 = - \sum_{\ell=2}^{NX2} (\ell-1)^2 B_{\ell j}^{-1} \cos(\ell-1) \psi_{o,k} \quad .$$

Substituting the partial derivatives in r_o and ψ_o directions into equation (2.2.7), the Laplace equation becomes the following system of second order ordinary differential equations in s_o :

$$\frac{d^2 \Omega_{ik}}{ds_o^2} = f_{ik}(\Omega_{nm}, f_3) \quad , \quad \begin{array}{l} i = 1, \dots, NX1 \\ k = 1, \dots, NX2 \end{array} \quad (2.2.51)$$

where f_{ik} is given by

$$f_{ik} = - \frac{(J_{ik})^2}{\alpha^2} \left\{ \frac{\partial^2 \Omega_{ik}}{\partial r_o^2} + \left(\frac{1}{r_{o,i}} + \frac{\alpha \cos \psi_{o,k}}{J_{ik}} \right) \frac{\partial \Omega_{ik}}{\partial r_o} \right. \\ \left. + \frac{1}{r_{o,i}^2} \frac{\partial^2 \Omega_{ik}}{\partial \psi_o^2} - \frac{\alpha \sin \psi_{o,k}}{J_{ik}} \frac{\partial \Omega_{ik}}{\partial \psi_o} \right\}$$

with

$$J_{ik} = 1 + \alpha r_{o,i} \cos \psi_{o,k} \quad .$$

The dependence on f_3 comes from equation (2.2.40).

The boundary conditions for (2.2.51) are

$$\frac{d\Omega_{ik}}{ds_0} = (f_1)_{ik} \quad \text{at} \quad s_0 = 0 \quad (2.2.52a)$$

and

$$\frac{d\Omega_{ik}}{ds_0} = (f_2)_{ik} \quad \text{at} \quad s_0 = \pi/2 \quad . \quad (2.2.52b)$$

System (2.2.51) with boundary conditions (2.2.52) constitutes a well posed boundary value problem. However, the solution can only be determined up to an arbitrary constant, as is well known from the mathematical theory of the Neumann problem for the Laplace equation. It is, of course, harmless since one is interested in the derivatives of Ω only. However, it does present a slight difficulty in obtaining numerical solution. The difficulty can be removed by assigning a value, say zero, to the potential function Ω at a particular point on the boundary or in the domain of interest. Alternatively, since the exit condition does not effect the initial development of the flow for most of the curved pipe, except near the exit region (as discussed before), we shall instead use the following exit condition:

$$\Omega = g(\psi_0, r_0) \quad \text{at} \quad s_0 = \pi/2 \quad , \quad (2.2.53)$$

where $g(\psi_0, r_0)$ is any prescribed function of ψ_0 and r_0 . Physically, (2.2.53) implies that the cross flow at the exit plane is given instead of the axial velocity.

The conventional Telenin's method transforms the boundary value problem into an initial value problem by guessing enough initial conditions to start the integration. These are then adjusted until the boundary conditions on the other side of the boundary are satisfied. This approach is analogous to the shooting method for solving a boundary value problem. Mathematically, one is trying to solve an elliptic problem by assigning Cauchy data along an initial line. This approach

suffers from the so-called Hadamard instability (Garabedian, 1964) which asserts that the solution of a Cauchy problem for an elliptic partial differential equation does not depend continuously on the initial data.

In view of this inherent instability of the conventional Telenin's method applied to an elliptic problem, one must use the fewest possible nodal points for the representation of the unknown and high precision computation. Furthermore, since one has to iterate on the initial data, the initial guesses must be close to the correct solution in order that the iteration converges. These requirements pose a serious limitation on the applicability of the conventional Telenin's method. Indeed, when the shooting technique was applied to system (2.2.51) subject to (2.2.53), solutions grew out of bound and it was not possible to iterate on the initial guesses. This can be due to the following. Since the present problem is three dimensional, the least number of nodes can be significant. For example, even though we have taken $NX1 = 3$ and $NX2 = 3$, the number of ordinary differential equations to be integrated is $2 \cdot NX1 \cdot NX2 = 18$. (The factor 2 accounts for the fact that (2.2.51) is a second order system.) The large number of differential equations makes it almost impossible to control the Hadamard instability. Furthermore, good initial guesses are difficult to make, which again amplifies the Hadamard instability even to a larger extent.

A different approach is sought by taking advantage of the linearity of system (2.2.51). Since Hadamard instability arises only when we try to cast the elliptic problem into a Cauchy initial value problem, numerical schemes based on the direct solution of (2.2.51) should eliminate the instability. To do so, let us divide the curved pipe into $NX3$ equal parts in the direction of increasing s_o , as shown in Fig. 3. Denote the value of Ω at the point (i,k) on the plane $s_o = (\frac{\nu}{NX3})^{\pi/2}$, where $\nu = 0, 1, \dots, NX3$,

by Ω_{ik}^v . (2.2.51) is then approximated by replacing the second derivative by a center difference formula. For the derivative boundary condition at $s_0 = 0$, we imagine a fictitious plane $s_0 = -(\frac{1}{NX3}) \cdot \frac{\pi}{2}$, and denote the values of Ω at this plane by Ω_{ik}^{-1} . A central difference scheme can be used to approximate the prescribed derivative boundary condition. In the case that the derivative condition is also prescribed at the exit (equation (2.2.52b)), it can be treated in a similar fashion. The resulting finite difference system of equation (2.2.51) is

$$\begin{aligned} \frac{\Omega_{ik}^{v-1} - 2\Omega_{ik}^v + \Omega_{ik}^{v+1}}{h^2} &= f_{ik}(\Omega_{nm}^v, f_3) \quad , \\ \frac{\Omega_{ik}^1 - \Omega_{ik}^{-1}}{2h} &= (f_1)_{ik} \quad , \\ \Omega_{ik} &= g_{ik} \quad \text{or} \quad \frac{\Omega_{ik}^{NX3+1} - \Omega_{ik}^{NX3-1}}{2h} = (f_2)_{ik} \quad , \end{aligned} \tag{2.2.54}$$

$$v = 0, 1, \dots, NX3 \quad , \quad i = 1, \dots, NX1 \quad , \quad k = 1, \dots, NX2 \quad ,$$

where $h = (\frac{1}{NX3})\frac{\pi}{2}$ is the step size in the present problem. Equation (2.3.54) is a linear system constituting $NX1 \cdot NX2 \cdot (NX3+1)$ algebraic equations for the unknowns Ω_{ik}^v at each node.

The linear system (2.2.54) has a very interesting property. Rearrangement of the equations enables us to write (2.2.54) in the following form

$$\underset{\sim}{A} \underset{\sim}{X} = \underset{\sim}{C} \quad , \tag{2.2.55}$$

where $\underset{\sim}{A}$ turns out to be a block tridiagonal matrix with the following special nature:

$$\underline{\underline{A}} = \begin{bmatrix} A_0 & 2I & & \\ I & A_1 & I & \\ & & A_v & \\ & & & nI & A_{NX3} \end{bmatrix} \quad (2.2.56)$$

with $A_0 = A_1 = \dots = A_{NX3}$ and I being the identity matrix. The order of each matrix element is $NX1 \cdot NX2$ by $NX1 \cdot NX2$. n is 1 when (2.2.53) is used and $n=2$ when (2.2.52b) is used. The transpose of $\underline{\underline{X}}$ is given by

$$\underline{\underline{X}}^T = \{X_0, X_1, \dots, X_{NX3}\} \quad , \quad (2.2.57)$$

where X_0 is a column vector containing Ω_{ik}^0 , $k=1, NX2$, $i=1, NX1$; X_1 containing Ω_{ik}^1 , etc.

Finally, $\underline{\underline{C}}$ contains the corresponding inhomogeneous term which depends on the boundary conditions. The special structure of the coefficient matrix $\underline{\underline{A}}$ improves the efficiency of the present numerical scheme for solving the Laplace equation tremendously. Thus, one can easily transform $\underline{\underline{A}}$ into a lower and upper triangular matrix as one does for an ordinary tridiagonal matrix (Issacson and Keller, 1966). The order of systems that need to be solved during the course of LU decomposition is at most $NX1 \cdot NX2$, as compared to the original order of $NX1 \cdot NX2 \cdot (NX3+1)$ in (2.2.54). Moreover, many matrix multiplications are saved since the lower and upper diagonal elements of $\underline{\underline{A}}$ are multiples of the identity matrix I .

The central difference scheme used is of order $O(h^2)$. Higher order difference approximations could be used to achieve higher accuracy for a fix h , but this will destroy the tridiagonal structure of $\underline{\underline{A}}$. Indeed, it is computationally more efficient to use a smaller h with central

difference than a bigger h with higher order difference.

Numerical Results and Discussion

The present modified version of Telenin's method was applied to solve the Laplace equation in a circular cylinder with prescribed Neumann boundary conditions, as shown in Fig. 4. It is worth mentioning that the solution shown in the figure was obtained with the full Neumann conditions, i.e., the solution could only be determined up to a constant. It is therefore surprising to find out that the numerical solution agrees closely with the exact solution. Possibly this is due to the approximate nature of the central difference scheme itself, so that the coefficient matrix of the system (2.2.54) is computationally nonsingular. In the limit $h \rightarrow 0$, one would expect to obtain a homogeneous system with a singular coefficient matrix. Other boundary conditions, mostly mixed Neumann-Dirichlet conditions for the same problem have been tried and in all cases there are close agreements between the numerical and exact solutions. Hence there is no doubt that the present modified scheme is more efficient than the conventional Telenin's method, at least when applied to a linear problem.

For the potential function in a curved pipe, exit condition (2.2.53) is used unless otherwise stated. Different forms of $g(r_o, \psi_o)$ have been tried and the solutions do not differ much from each other over most of the curved pipe downstream of the entry plane. This is in conformity with the matched asymptotic expansion solution derived before. In view of this, we take $g = \text{constant}$, which corresponds to vanishing cross flow at the exit plane. This is a reasonable choice since the cross flow in the whole domain of interest is small compared to the axial motion for small α .

Figures 5 to 8 present the numerical solution of the potential function in a curved tube. The velocity components are obtained from equation (2.2.6), together with the interpolation functions chosen for the representation of Ω . The mesh size in the core region is given by $NX1 = 3$ and $NX2 = 5$ throughout the whole analysis.

Figure 5a shows the velocity potential, normalized as indicated in the figure solely for graphing purposes, at the entry plane of a curved pipe with $\alpha = 0.1$. The slight variation of Ω reflects a corresponding slight cross flow at the entry superimposed on the uniform entry profile. In this context, it is worthwhile to mention that one may not in general prescribe all three velocity components on the entry plane, since this will fix both Ω and its normal derivative $\frac{\partial \Omega}{\partial s_0}$, and the elliptic problem becomes ill posed. This cross flow decays quite fast downstream, and Ω becomes uniform over the cross flow plane when $s_0 = 0.1\pi$ is reached, as shown in Fig. 5b.

Figure 6 shows the variation of Ω along the curved pipe for two values of the curvature ratio, α . The uniform exit condition (2.2.52b) was used. It can be seen that Ω is essentially a function of s_0 when $\alpha = 0.1$. Moreover, it corresponds almost to the velocity potential of a two-dimensional point vortex given by

$$\Omega = C_2 s_0, \quad (2.2.58)$$

where C_2 is given in (2.2.25). It can easily be shown that

$$C_2 = 1 + \frac{\pi}{8} \alpha^2 + O(\alpha^4)$$

so that for $\alpha = 0.1$, $C_2 \approx 1$. This agrees with the matched asymptotic solution obtained in Section 2.2.

For $\alpha = 0.6$, the variation of Ω in the cross flow directions is more pronounced, albeit the absolute magnitudes of the variation are still small. This is expected because the inner regions (both near the entry and the exit) cover a much larger distance (roughly of $O(\alpha)$). Hence the conditions on the entry and exit planes persist further downstream/upstream of the entry/exit planes.

The cross flow velocity component parallel to the plane of symmetry is next shown in Fig. 7(a) and 7(b) for $\alpha = 0.1$. It is indeed very small and can safely be neglected as compared to the streamwise velocity component, which is shown in Fig. 8(a) and 8(b) at two stations downstream of the entry location. The entry profile is also shown for comparison. It can be seen that the flow almost develops into the corresponding vortex flow at $s_0 = (0.1)\frac{\pi}{2}$ and is fully developed when it reaches $s_0 = (0.2)\frac{\pi}{2} = 3.14\alpha$. This is also in qualitative agreement with Agrawal, Talbot and Gong, whose measurement indicates the potential vortex is fully developed at a station $s_0 = 2.4\alpha$.

The above discussion has been carefully restricted to the very early development of the flow. Hence it is still valid even when viscosity effect is accounted for. Further downstream, the interaction of the core flow with the boundary layer may alter the core flow behavior. The main effects of the boundary layer on the outer flow are twofold: firstly, the boundary layer thickness reduces the effective cross section of the inviscid region and secondly, the normal velocity on the pipe wall (or more precisely, on the outer edge of the boundary layer) for the outer flow is no longer vanishing, as was assumed earlier. Of course, these two effects are minute in the very beginning of the flow development compared to the later stages of the entry flow.

2.3 Flow inside the boundary layer

As fluid enters the curved pipe, a boundary layer forms all around the pipe circumference as in a straight pipe and grows downstream. Since the Dean number in the present study is large, the boundary layer will remain thin as the flow approaches the fully developed state. Under such circumstances, it is advantageous to apply boundary layer theory to the full Navier-Stokes equations near the pipe wall.

By means of an order of magnitude analysis, one can readily obtain the boundary layer equations in the entry region of a curved pipe.

Introducing the following dimensionless quantities

$$U = \frac{uD^{\frac{1}{2}}}{W_e}, \quad V = \frac{v}{W_e}, \quad W = \frac{w}{W_e}, \quad P = \frac{p}{\rho W_i^2}, \quad W_e = \frac{w_e}{W_i}, \quad (2.3.1)$$

$$\eta = (a-r)D^{\frac{1}{2}}/a, \quad \psi = \psi, \quad s = \frac{\phi}{\alpha}, \quad (2.3.2)$$

where α is the curvature ratio of the curved tube. Subscript e refers to quantities at the outer edge of the boundary layer and W_i is the constant entry velocity as defined before. The boundary layer equations can then be expressed as follows:

$$\frac{\partial P}{\partial \eta} = 0, \quad (2.3.3)$$

$$\begin{aligned} -U \frac{\partial V}{\partial \eta} + V \frac{\partial V}{\partial \psi} + \frac{W}{1+\alpha \cos \psi} \frac{\partial V}{\partial s} + \frac{\alpha W^2 \sin \psi}{1+\alpha \cos \psi} + \left\{ V^2 \frac{\partial W_e}{\partial \psi} + \frac{WV}{1+\alpha \cos \psi} \frac{\partial W_e}{\partial s} \right\} \frac{1}{W_e} \\ = -\frac{1}{W_e^2} \frac{\partial P}{\partial \psi} + \frac{\sqrt{\alpha}}{W_e} \frac{\partial^2 V}{\partial \eta^2}, \end{aligned} \quad (2.3.4)$$

$$\begin{aligned} -U \frac{\partial W}{\partial \eta} + V \frac{\partial W}{\partial \psi} + \frac{W}{1+\alpha \cos \psi} \frac{\partial W}{\partial s} - \frac{\alpha VW \sin \psi}{1+\alpha \cos \psi} + \left\{ \frac{VW}{W_e} \frac{\partial W_e}{\partial \psi} + \frac{W^2}{W_e(1+\alpha \cos \psi)} \frac{\partial W_e}{\partial s} \right\} \\ = -\frac{1}{1+\alpha \cos \psi} \frac{1}{W_e^2} \frac{\partial P}{\partial s} + \frac{\sqrt{\alpha}}{W_e} \frac{\partial^2 W}{\partial \eta^2}. \end{aligned} \quad (2.3.5)$$

The continuity equation becomes

$$-\frac{\partial U}{\partial \eta} + \frac{\partial V}{\partial \psi} + \frac{1}{1+\alpha \cos \psi} \frac{\partial W}{\partial s} - \frac{\alpha V \sin \psi}{1+\alpha \cos \psi} + \left\{ \frac{V}{W_e} \frac{\partial W_e}{\partial \psi} + \frac{W}{W_e (1+\alpha \cos \psi)} \frac{\partial W_e}{\partial s} \right\} = 0 \quad (2.3.6)$$

In deriving equations (2.3.3) to (2.3.6), the radial coordinate r is approximated by the radius of the pipe, a , since the boundary layer is assumed thin compared to the radius. By virtue of (2.3.3), the pressure in the boundary layer is imposed by the outer flow, i.e., the inviscid core. It can be easily written in terms of the outer boundary layer edge velocity components by neglecting the viscous terms in (2.3.4) and (2.3.5). Remembering $\frac{\partial V}{\partial \eta}$ and $\frac{\partial W}{\partial \eta}$ vanish at the outer edge, we obtain, for the pressure gradients

$$-\frac{1}{W_e^2} \frac{\partial P}{\partial \psi} = V_e \frac{\partial V_e}{\partial \psi} + \frac{1}{1+\alpha \cos \psi} \frac{\partial V_e}{\partial s} + \frac{\alpha \sin \psi}{1+\alpha \cos \psi} + \frac{1}{W_e} \left\{ V_e^2 \frac{\partial W_e}{\partial \psi} + \frac{V_e}{1+\alpha \cos \psi} \frac{\partial W_e}{\partial s} \right\} \quad (2.3.7)$$

and

$$-\frac{1}{1+\alpha \cos \psi} \frac{1}{W_e^2} \frac{\partial P}{\partial s} = -\frac{\alpha V_e \sin \psi}{1+\alpha \cos \psi} + \left\{ V_e \frac{\partial W_e}{\partial \psi} + \frac{1}{1+\alpha \cos \psi} \frac{\partial W_e}{\partial s} \right\} \frac{1}{W_e} \quad (2.3.8)$$

The boundary conditions are now

$$U = V = W = 0 \quad \text{at} \quad \eta = 0, \quad (2.3.9)$$

$$U = U_e, \quad V = V_e, \quad W = 1, \quad \frac{\partial U}{\partial \eta} = \frac{\partial V}{\partial \eta} = \frac{\partial W}{\partial \eta} = 0, \quad \eta \rightarrow \infty$$

and U, V, W given at $s = s_1$, an appropriate initial station.

Method of integral relations as applied to the boundary layer equations

Originally formulated by Dorodnitsyn (1956), the Method of Integral Relations (M.I.R.) has been applied to a wide variety of current problems in fluid mechanics which are governed by partial differential equations of elliptic, mixed elliptic-hyperbolic, or parabolic type. The key feature of this method is to reduce the number of independent variables

by one, so that, in problems involving only two independent variables, the reduced system consists of ordinary differential equations. When M.I.R. is applied to the boundary layer equation (Dorodnitsyn, 1960), the normal coordinate is replaced by the streamwise velocity component, similar to the well-known Crocco's transformation. Recently, Modarress (1978) has applied M.I.R. to solve the three-dimensional boundary layer equations. Both separating and non-separating flows were considered. A full description of M.I.R. and related applications can be found in Holt (1977).

Mathematically, M.I.R. distinguishes itself from other standard integral methods, such as the Karman-Pohlhausen method, in that M.I.R. guarantees the convergence of the approximate solution, at least in principle (Abbott and Bethel, 1968). Shiau and Yeung (1978, unpublished) have applied the method of integral relations to solve the fully developed curved pipe flow. They obtained a resistance coefficient formula which agrees well with experimental results. It is thus desirable to extend the method to the entry region. We shall now proceed to derive the basic integral relations.

The first integral relation is obtained by multiplying equation (2.3.6) by $g_k(W)$, equation (2.3.5) by $g'_k(W)$, add and integrate the result with respect to η from 0 to ∞ . Then change the variable of integration to W by introducing a new dependent variable Z , where

$$Z = (\partial W / \partial \eta)^{-1} \quad (2.3.10)$$

$\{g_k(W)\}$ is a complete set of linearly independent functions the elements of which satisfy the condition

$$\lim_{W \rightarrow 1} g_k(W) = 0, \quad \forall k. \quad (2.3.11)$$

The exact form of $g_k(W)$ will be discussed later. The prime denotes differentiation with respect to W . We obtain

$$\begin{aligned} & \frac{\partial}{\partial \psi} \int_0^1 V Z g_k dW + \frac{1}{1+\alpha \cos \psi} \frac{\partial}{\partial s} \int_0^1 W Z g_k dW \\ &= \left(\frac{\alpha \sin \psi}{1+\alpha \cos \psi} - \frac{1}{W_e} \frac{\partial W_e}{\partial \psi} \right) \int_0^1 [(VW - V_e) g_k' + V g_k] Z dW \\ &+ \frac{1}{1+\alpha \cos \psi} \frac{1}{W_e} \frac{\partial W_e}{\partial s} \int_0^1 [(1-W^2) g_k' - W g_k] Z dW - \frac{\sqrt{\alpha}}{W_e} \frac{g_k'(0)}{Z_0} - \frac{\sqrt{\alpha}}{W_e} \int_0^1 \frac{g_k''}{Z} dW . \quad (2.3.12) \end{aligned}$$

Equation (2.3.8) has been used to replace $\partial P / \partial s$. Z_0 is the value of Z at the wall, i.e., $\eta = 0$.

The second integral relation is derived by transforming (η, ψ, s) to (W, ψ, s) in equation (2.3.4). The following rules of transformation hold

$$\begin{aligned} \left(\frac{\partial V}{\partial \eta} \right)_{\psi, s} &= \left(\frac{\partial V}{\partial W} \right)_{\psi, s} \left(\frac{\partial W}{\partial \eta} \right)_{\psi, s} , \\ \left(\frac{\partial V}{\partial \psi} \right)_{\eta, s} &= \left(\frac{\partial V}{\partial \psi} \right)_{W, s} \left(\frac{\partial \psi}{\partial \psi} \right)_{\eta, s} + \left(\frac{\partial V}{\partial W} \right)_{\psi, s} \left(\frac{\partial W}{\partial \psi} \right)_{\eta, s} , \\ \left(\frac{\partial V}{\partial s} \right)_{\eta, \psi} &= \left(\frac{\partial V}{\partial s} \right)_{W, \psi} \left(\frac{\partial s}{\partial s} \right)_{\eta, \psi} + \left(\frac{\partial V}{\partial W} \right)_{\psi, s} \left(\frac{\partial W}{\partial s} \right)_{\eta, \psi} , \\ \frac{\partial^2 V}{\partial \eta^2} &= \left(\frac{\partial^2 V}{\partial W^2} \right)_{\psi, s} \left(\frac{\partial W}{\partial \eta} \right)_{\psi, s}^2 + \left(\frac{\partial V}{\partial W} \right)_{\psi, s} \left(\frac{\partial^2 W}{\partial \eta^2} \right)_{\psi, s} . \end{aligned} \quad (2.3.13)$$

With the help of (2.3.5), the transformed equation, factored by a weighting function $h_k(W)$, is integrated with respect to W from 0 to 1. Finally equation (2.3.7) is used for the pressure gradient term and the following results:

$$\begin{aligned}
& \frac{\partial}{\partial \psi} \int_0^1 \frac{V^2}{2} h_k dW + \frac{1}{1+\alpha \cos \psi} \frac{\partial}{\partial s} \int_0^1 W V h_k dW = \frac{1}{W_e} \frac{\partial W_e}{\partial \psi} \int_0^1 \{ (V_e^2 - V^2) - \frac{\partial V}{\partial W} (V_e - VW) \} h_k(W) dW \\
& + \frac{1}{1+\alpha \cos \psi} \frac{1}{W_e} \frac{\partial W_e}{\partial s} \int_0^1 \{ V_e - WV - \frac{\partial V}{\partial W} (1-W^2) \} h_k dW \\
& + \frac{\alpha \sin \psi}{1+\alpha \cos \psi} \int_0^1 (1-W^2) - \frac{\partial V}{\partial W} (VW - V_e) \} h_k(W) dW \\
& + (V_e \frac{\partial V_e}{\partial \psi} + \frac{1}{1+\alpha \cos \psi} \frac{\partial V_e}{\partial s}) \int_0^1 h_k(W) dW + \frac{\sqrt{\alpha}}{W_e} \int_0^1 \frac{\partial^2 V}{\partial W^2} \frac{1}{Z^2} h_k(W) dW \quad (2.3.14)
\end{aligned}$$

bearing in mind that $\frac{\partial}{\partial \psi}$ and $\frac{\partial}{\partial s}$ here imply keeping W constant. $\{h_k(W)\}$ is again a set of linearly independent functions; however, no special requirement must be satisfied by $h_k(W)$.

On the plane of symmetry, $\psi = 0$ and $\psi = \pi$, equation (2.3.12) can be simplified by asserting that $V = 0$ and $\frac{\partial Z}{\partial \psi} = 0$ to obtain

$$\begin{aligned}
\frac{1}{1+\alpha \cos \psi} \frac{d}{ds} \int_0^1 W Z dW = & - \int_0^1 Z S g_k dW + \frac{1}{1+\alpha \cos \psi} \frac{1}{W_e} \frac{dW_e}{ds} \int_0^1 [(1-W^2) g_k' - W g_k] Z dW \\
& - \frac{\sqrt{\alpha} g_k'(0)}{W_e Z_0} - \frac{\sqrt{\alpha}}{W_e} \int_0^1 \frac{g_k''}{Z} dW \quad , \quad (2.3.15)
\end{aligned}$$

where the new variable S is defined as

$$S = \frac{\partial V}{\partial \psi} \quad . \quad (2.3.16)$$

Next, we differentiate equation (2.3.14) with respect to ψ , imposing the symmetry conditions, and obtain

$$\begin{aligned}
\frac{1}{1+\alpha \cos \psi} \frac{d}{ds} \int_0^1 W S h_k dW = & - \int_0^1 S^2 h_k dW + \frac{1}{1+\alpha \cos \psi} \frac{1}{W_e} \frac{dW_e}{ds} \int_0^1 [(S_e - WS) - \frac{\partial S}{\partial W} (1-W^2)] h_k dW \\
& + \frac{\alpha \cos \psi}{1+\alpha \cos \psi} \int_0^1 (1-W^2) h_k dW + (S_e^2 + \frac{1}{1+\alpha \cos \psi} \frac{dS_e}{ds}) \int_0^1 h_k dW \\
& + \frac{\sqrt{\alpha}}{W_e} \int_0^1 \frac{\partial^2 S}{\partial W^2} \frac{1}{Z^2} h_k dW \quad , \quad (2.3.17)
\end{aligned}$$

where S_e stands for $\partial V_e / \partial \psi$, in accordance with (2.3.16). Thus, the basic integral relations reduce to ordinary differential equations on the plane of symmetry in the variables Z and S . The boundary condition on S can be readily deduced as

$$S = 0 \quad \text{at} \quad W = 0$$

and

$$S = S_e \quad \text{at} \quad W = 1 \quad .$$

(2.3.18)

To solve equations, say (2.3.12) and (2.3.14), we represent the unknowns analytically, in the form of a series based on some complete system of functions. Conventionally, simple power series in the integration variable, W , is assumed for the reciprocal of shear stress, Z , and V ; the integrals in the integral relations are then evaluated analytically and the resulting system of partial differential equations are solved numerically. The amount of algebra involved is tremendous and the coefficient matrix for the resulting system of differential equations becomes more ill-behaved as one tries higher approximations. In an attempt to overcome these difficulties, Fletcher and Holt (1976) developed an orthonormal version of M.I.R. It has been successfully applied to nonseparating flows, all of which involve only two independent variables. We shall apply this modified version of M.I.R. to the present three-dimensional problem.

The basic idea is to choose sets of orthonormal functions for the weighting functions ($g(W)$ and $h(W)$). The integrands on the left-hand side of (2.3.12) and (2.3.14) are then expressed in terms of these orthonormal functions. Using the orthogonality conditions, one can evaluate quite straightforwardly the left-hand side of (2.3.12) and (2.3.14). The corresponding right-hand sides are evaluated numerically rather than analytically.

For problems where only two independent variables are involved, the number of unknown integrands that are preceded by a differential operator is the same as the number of integral relations derived. Moreover, each dependent variable (Z or V) can be solved uniquely from these unknown integrands (see, for example, Fletcher and Holt, 1976). However, this is not true for the present three-dimensional problem. Indeed, there are four unknown integrands (VZ, WZ, V^2 and WV) and only two integral relations. This is, of course, due to the dependence on one more coordinate of the flow variables. To circumvent this difficulty, we rewrite (2.3.12) and (2.3.14) respectively as follows:

$$\frac{1}{1+\alpha \cos \psi} \frac{\partial}{\partial s} \int_0^1 WZ g_k dW = C(k) - \int_0^1 \left(V \frac{\partial Z}{\partial \psi} + Z \frac{\partial V}{\partial \psi} \right) g_k dW, \quad (2.3.19)$$

$$\frac{1}{1+\alpha \cos \psi} \frac{\partial}{\partial s} \int_0^1 WV h_k dW = D(k) - \int_0^1 V \frac{\partial V}{\partial \psi} h_k dW, \quad (2.3.20)$$

where $D(k)$ and $D(k)$ represent the right-hand sides of (2.3.12) and (2.3.14) respectively. Here k denotes the subscript on the orthonormal function $g(W)$ or $h(W)$.

In the N th approximation, Z and V are represented as

$$Z = \{b_{o1} + \sum_{j=1}^{N-1} b_{j1} g_j(W)\} / (1-W), \quad (2.3.21)$$

$$V = \{V_e + \sum_{j=1}^N b_{j2} h_j(W)\} W. \quad (2.3.22)$$

To satisfy condition (2.3.11), the $g_k(W)$ is chosen as

$$g_k(W) = \sum_{j=1}^k a_{kj} (1-W)^j, \quad (2.3.23)$$

where the coefficients a_{kj} are determined from the orthogonality condition imposed on $g_k(W)$

$$\int_0^1 g_i(W) g_j(W) \frac{W}{1-W} dW = \delta_{ij} \quad , \quad (2.3.24)$$

δ_{ij} is the Kronecker delta. Since there is no special requirement on $h_k(W)$, one can use any orthonormal set with an appropriate weighting function. However, from (2.3.22), the boundary conditions on V ($V=0$ at $W=0$ and $V=V_e$ at $W=1$) can be satisfied automatically if we choose $h_k(W)$ as a linear combination of the functions $\{(1-W)^j, j=1, \dots, k\}$ also. Thus,

$$h_k(W) = \sum_{j=1}^k c_{kj} (1-W)^j \quad . \quad (2.3.25)$$

The coefficients c_{kj} are now determined from the condition

$$\int_0^1 W^2 h_i(W) h_j(W) dW = \delta_{ij} \quad . \quad (2.3.26)$$

Notice that the weighting functions for $g(W)$ and $h(W)$ are different even though their representations are similar. The existence and uniqueness of such orthonormal functions are the content of the Gram-Schmidt process (Issacson and Keller, 1966). Clearly

$$g_k(1) = h_k(1) = 0 \quad , \quad \forall k \quad . \quad (2.3.27)$$

Substituting (2.3.21) into equation (2.3.19) and using (2.3.24) we obtain

$$\frac{1}{1+\alpha \cos \psi} \left\{ \frac{\partial b_{01}}{\partial s} \int_0^1 \frac{W g_k(W)}{1-W} dW + \frac{\partial b_{j1}}{\partial s} \right\} = C(k) - \int_0^1 \left(V \frac{\partial Z}{\partial \psi} + Z \frac{\partial V}{\partial \psi} \right) g_k(W) dW \quad ,$$

$$k=1, \dots, N-1 \quad ,$$

$$\frac{1}{1+\alpha \cos \psi} \frac{\partial b_{01}}{\partial s} \int_0^1 \frac{W g_N(W)}{1-W} dW = C(N) - \int_0^1 \left(V \frac{\partial Z}{\partial \psi} + Z \frac{\partial V}{\partial \psi} \right) g_N(W) dW \quad , \quad k=N$$

We can further simplify the above by substituting $\partial b_{01}/\partial s$ to obtain

$$\frac{\partial b_{o1}}{\partial s} = \frac{\bar{C}(N)(1+\alpha \cos \psi)}{\int_0^1 \frac{W g_N(W)}{1-W} dW} ,$$

and

$$\frac{1}{1+\alpha \cos \psi} \frac{\partial b_{k1}}{\partial s} = \bar{C}(k) - \frac{\bar{C}(N) \int_0^1 \frac{W g_k(W)}{1-W} dW}{\int_0^1 \frac{W g_N(W)}{1-W} dW} , \quad k=1, \dots, N-1 \quad (2.3.28)$$

where

$$\bar{C}(\ell) \equiv C(\ell) - \int_0^1 (V \frac{\partial Z}{\partial \psi} + Z \frac{\partial V}{\partial \psi}) g_\ell(W) dW , \quad \ell=1, 2, \dots, N . \quad (2.3.29)$$

Similarly, equation (2.3.20) gives

$$\frac{1}{1+\alpha \cos \psi} \frac{\partial b_{k2}}{\partial s} = \bar{D}(k) - \frac{1}{1+\alpha \cos \psi} \frac{\partial V_e}{\partial s} \int_0^1 W^2 h_k(W) dW , \quad k=1, \dots, N \quad (2.3.30)$$

where

$$\bar{D}(\ell) \equiv D(\ell) - \int_0^1 V \frac{\partial V}{\partial \psi} h_\ell(W) dW , \quad \ell=1, 2, \dots, N . \quad (2.3.31)$$

Equations (2.3.28) and (2.3.30) constitute 2N coupled partial differential equations in s and ψ , which can be solved for the 2N unknown coefficients introduced in (2.3.21) and (2.3.22).

Similarly, on the plane of symmetry, $\psi=0$ and $\psi=\pi$, exactly the same approach applied to equations (2.3.15) and (2.3.17) yields the following system

$$\begin{aligned} \frac{db_{o1}}{ds} &= \frac{\tilde{C}(N)(1+\alpha \cos \psi)}{\int_0^1 \frac{W g_N(W)}{1-W} dW} , \\ \frac{1}{1+\alpha \cos \psi} \frac{db_{k1}}{ds} &= \tilde{C}(k) - \frac{\tilde{C}(N) \int_0^1 \frac{W g_k(W)}{1-W} dW}{\int_0^1 \frac{W g_N(W)}{1-W} dW} , \\ \frac{1}{1+\alpha \cos \psi} \frac{de_k}{ds} &= \tilde{D}(k) - \frac{1}{1+\alpha \cos \psi} \frac{ds_e}{ds} \int_0^1 W^2 h_k(W) dW , \end{aligned} \quad (2.3.32)$$

where now $\tilde{C}(k)$ and $\tilde{D}(k)$ represent the right-hand sides of equations (2.3.15) and (2.3.17) respectively and e_k is the k th coefficient in the approximate representation of S , given below:

$$S = [S_e + \sum_{j=1}^N e_j h_j(W)]W \quad . \quad (2.3.33)$$

Initial conditions

In the immediate neighborhood of the entry section, the curved pipe behaves like a straight pipe. Thus, the correct initial conditions must be obtained from the solution of the uniform entry into a straight tube. To a first approximation, we can use the Blasius solution with a free stream velocity equal to W_i (i.e., $W_e = 1$). In order to apply the integral relations in this region, we need to rewrite the boundary layer equations in cylindrical coordinates, with the center of the entry plane as the origin and the z axis in the direction of the entry flow. This can be easily accomplished by setting $\alpha = 0$ and redefining the parameter Z as

$$\tilde{Z} = \left(\frac{\partial W}{\partial \tilde{\eta}}\right)^{-1} \quad , \quad \tilde{\eta} = \frac{a-r}{a} \text{Re}^{\frac{1}{2}} \quad . \quad (2.2.34)$$

Equation (2.3.12) becomes

$$\frac{\partial}{\partial z} \int_0^1 W \tilde{Z} g_k dW = - \frac{g'_k(0)}{\tilde{Z}} - \int_0^1 \frac{g''_k}{\tilde{Z}} dW \quad (2.3.35)$$

and the azimuthal velocity component is

$$V = 0 \quad . \quad (2.3.36)$$

\tilde{Z} is related to Z by the following

$$\tilde{Z} = Z \alpha^{-\frac{1}{4}} \quad . \quad (2.3.37)$$

From the Blasius solution, we can express W as

$$W = W(\zeta) \quad ,$$

where ζ is the Blasius variable

$$\zeta = \frac{\tilde{\eta}}{\sqrt{2z}} \quad .$$

Hence

$$1/\tilde{Z} = \frac{\partial W}{\partial \tilde{\eta}} = \frac{\partial \zeta}{\partial \tilde{\eta}} W'(\zeta) = \frac{1}{\sqrt{2z}} W'(\zeta) = \frac{\theta(\zeta)}{\sqrt{z}} \quad .$$

Since W is a function of ζ only, when W is constant ζ is also constant, so that we may write, on the i -th W boundary

$$\tilde{Z}_j = \theta_j \sqrt{z} \quad \text{and} \quad \tilde{Z} = \theta(W) \sqrt{z} \quad , \quad (2.3.38)$$

where Z_j is the value of Z at $W = \frac{i}{N}$ and θ_j 's are constants. The application of the method of integral relations to the flow defined by (2.3.36) and (2.3.38) yields a system of nonlinear coupled algebraic equations in θ_j , $j = 0, \dots, N-1$, whose solutions can be obtained readily.

For the orthonormal M.I.R., one cannot in general solve directly for the θ_j 's because the fundamental variables involved in equations (2.3.28) and (2.3.30) are not the value of Z at each W boundary. In fact, they are linear combinations of the Z_j 's as seen from equation (2.3.21). Thus, one may write down the coefficients b_{0l} , $\{b_{jl}\}$ symbolically as

$$b_{0l} = \sum_{j=0}^{N-1} \alpha^{\frac{1}{4}} d_{0j} \tilde{Z}_j \quad , \quad (2.3.39)$$

$$b_{kl} = \sum_{j=0}^{N-1} \alpha^{\frac{1}{4}} d_{kj} \tilde{Z}_j \quad , \quad k = 1, \dots, N-1 \quad ,$$

where equation (2.3.37) is used. From equation (2.3.38) it follows that

b_{01} , $\{b_{kl}\}$ have the same square root dependence on z , so that we may write

$$\begin{aligned} b_{01} &= \alpha^{\frac{1}{4} \bar{A}_0} \sqrt{z} \quad , \\ b_{kl} &= \alpha^{\frac{1}{4} \bar{A}_k} \sqrt{z} \quad , \quad k=1, \dots, N-1 \quad , \end{aligned} \quad (2.3.40)$$

where

$$\bar{A}_0 = \sum_{j=1}^{N-1} d_{0j} \theta_j \quad , \quad \bar{A}_k = \sum_{j=0}^{N-1} d_{kj} \theta_j \quad . \quad (2.3.41)$$

Substitution of (2.3.40) into equation (2.3.28) yields the following:

$$\begin{aligned} \frac{1}{2} \bar{A}_0 &= \frac{S(N)}{\int_0^1 \frac{W g_N}{1-W} dW} \quad , \\ \frac{1}{2} \bar{A}_k &= S(k) - \frac{S(N) \int_0^1 \frac{W g_k}{1-W} dW}{\int_0^1 \frac{W g_N}{1-W} dW} \quad , \quad k=1, \dots, N-1 \quad , \end{aligned} \quad (2.3.42)$$

where

$$S(\ell) = -\frac{g'_\ell(0)}{\theta_0} - \int_0^1 \frac{g''_\ell}{\theta(W)} dW \quad , \quad \ell=1, \dots, N \quad .$$

Substituting (2.3.40) into equation (2.3.21) and comparing with equation (2.3.38), we find that

$$\theta(W) = \{\bar{A}_0 + \sum_{j=1}^{N-1} \bar{A}_j g_j(W)\} / (1-W) \quad (2.3.43)$$

and hence

$$\theta_0 = \{\bar{A}_0 + \sum_{j=1}^{N-1} \bar{A}_j g_j(0)\} \quad . \quad (2.3.44)$$

System (2.3.42) consists of N coupled algebraic equations in N unknowns \bar{A}_0, \bar{A}_k , $k=1, \dots, N-1$, whose solution in general can only be found iteratively. Having found the \bar{A} 's, equation (2.3.40) can be used to evaluate

the initial values of b_{01} , $\{b_{k1}\}$ at an initial station z_1 . The initial conditions for $\{b_{j2}, j=1, \dots, N\}$ are, from (2.3.36)

$$b_{j2} = 0, \quad j=1, \dots, N. \quad (2.3.45)$$

The initial condition at the plane of symmetry for the unknown S can be easily derived from (2.3.36) as

$$S = \frac{\partial V}{\partial \psi} = 0,$$

so that we have

$$e_j = 0, \quad j=1, \dots, N. \quad (2.3.46)$$

Numerical investigation of the boundary layer equations

In general, the method of integral relations reduces the three-dimensional parabolic boundary layer equations to a system of first order, hyperbolic partial differential equations, with initial conditions derived in the last section. To solve this system numerically, it is necessary to approximate the derivatives by some sort of finite difference formulae. Alternatively, one can, of course, apply the same idea with Telenin's method. Thus, for example, one can represent the unknowns by suitable interpolating functions in the aximuthal direction (ψ) and evaluate the cross derivatives (i.e., ψ derivatives) analytically. The resulting equations can then be integrated in the streamwise direction. However, it was found that such approach yielded results that were oscillatory with the streamwise variable, s , when the number of points in the ψ direction exceeded three. The same phenomenon was also reported by Modarress (1974), who pointed out that since the reduced boundary layer equations are of hyperbolic type, the cross derivative at any point should only depend on the values of the unknowns at neighboring points.

In view of the unstable nature of Telenin's method when applied to the present problem, backward difference for the cross derivatives was used and was found to be successful. It should be mentioned that the instability encountered here is not the Hadamard instability encountered before in the core region. Indeed, the Hadamard instability is not relevant here because the integral relations are of hyperbolic type. If we divide the ψ domain into ℓ equal intervals, the cross derivative of any unknown f at the nodal point $\psi_k = k\pi/\ell$, $k=1,2,\dots,(\ell-1)$ is given by

$$\left(\frac{\partial f}{\partial \psi}\right)_k = \frac{f_k - f_{k-1}}{\Delta \psi}, \quad (2.3.47)$$

where f_k and f_{k-1} are the values of f at ψ_k and ψ_{k-1} , respectively, and $\Delta \psi$ is simply

$$\Delta \psi = \frac{\pi}{\ell}. \quad (2.3.48)$$

On the plane $\psi = 0$, the solution can be obtained independently from the rest of the planes $\psi = \psi_k$, $k=1,\dots,(\ell-1)$ by integrating simultaneously the modified M.I.R. equations (c.f. equations (2.3.32)). Solution at this plane can be used to calculate the cross derivatives of the next plane, and so on until the last plane is reached. At each plane, there are $2N$ integral relations from either equations (2.3.28) and (2.3.30), or equations (2.3.32), so that in the N th approximation, there are in total $2N \cdot (\ell+1)$ coupled ordinary differential equations in the unknowns $\{e_j, j=1,\dots,N\}$, $\{b_{j1}, j=0,\dots,N-1\}$ and $\{b_{j2}, j=1,\dots,N\}$.

It is worth mentioning that the symmetry equations are not used on the plane $\psi = \pi$ because it has been found that a very small step size has to be used for the integration of equations (2.3.32). The unknown S is found to attain large negative values as the flow moves downstream.

This is supplemented by the fact that the inverse shear stress Z also increases very fast at the inner bend, $\psi = \pi$. The combined effect renders equation (2.3.32) at $\psi = \pi$ not so well behaved from a numerical viewpoint because the magnitude of some of the terms on the right-hand side of (2.3.32) may become too large, and the significance of other terms will be lost during computation. In this sense, equations (2.3.28) and (2.3.30) are more well behaved because the azimuthal velocity, V , at $\psi = \pi$ is zero along the whole pipe.

The remaining task is to supply an appropriate outer (core) solution in order to evaluate the velocity components and their gradients at the outer edge of the boundary layer ($V_e, W_e, \frac{\partial W_e}{\partial \psi}$, etc.). However, the outer solution in turn depends on the boundary layer solution. Before discussing the interaction between the two solutions, which will be the subject matter of the next section, let us derive the expressions for the velocity components and the displacement thickness from the boundary layer solution.

We shall define the displacement thickness as follows:

$$\delta_1 = \int_0^\infty (1-W) d(a-r)$$

and in the present notation,

$$\frac{\delta_1}{a} = \frac{1}{D^{\frac{1}{2}}} \int_0^1 (1-W) Z dW \quad . \quad (2.3.49)$$

From the representation of Z , or $\frac{\partial \eta}{\partial W}$, the displacement thickness can be given in closed form in terms of the coefficients b_{kl} :

$$\frac{\delta_1}{a} = \frac{1}{D^{\frac{1}{2}}} \left\{ b_{01} + \sum_{j=1}^{N-1} b_{j1} \cdot \sum_{\ell=1}^j a_{j\ell} \left(\frac{1}{\ell+1} \right) \right\} \quad , \quad (2.3.50)$$

$a_{j\ell}$ being the coefficients of the orthonormal functions $\{g\}$ in (2.3.23).

For the streamwise velocity component W , it can be determined from

the representation of Z . In the N th approximation, we have

$$\eta = \int_0^W Z dW = \int_0^W \frac{b_{01} + \sum_{j=1}^{N-1} b_{j1} g_j(\tilde{W})}{1 - \tilde{W}} d\tilde{W} . \quad (2.3.51)$$

The integral on the right can also be evaluated in a closed form. The final result is

$$\eta = -b_{01} \ln(1-W) + \sum_{j=1}^{N-1} b_{j1} \cdot \sum_{k=1}^j a_{jk} \cdot \sum_{n=1}^k (-1)^{n-1} \binom{k}{n} \frac{W^n}{n} , \quad (2.3.52)$$

where

$$\binom{k}{n} = \frac{k!}{n!(k-n)!} .$$

The inverse of (2.3.52) can only be obtained numerically for $n \geq 3$.

Nevertheless, (2.3.52) provides the streamwise velocity profile in the physical coordinate, η .

The azimuthal velocity profile, V , in the physical coordinate can be obtained from (2.3.9) and (2.3.6) and is given symbolically as

$$V(\eta) = \{V_e + \sum_{j=1}^N b_{j2} h_j(W(\eta))\} W(\eta) . \quad (2.3.53)$$

It should be realized that V and W depend on ψ and s as well.

Finally, for the radial velocity component, one obtains by integrating the continuity equation, equation (2.3.6)

$$\begin{aligned} U = \int_0^\eta \left(\frac{\partial V}{\partial \psi} \right) d\eta + \frac{1}{1+\alpha \cos \psi} \int_0^\eta \frac{\partial W}{\partial s} d\eta - \frac{\alpha \sin \psi}{1+\alpha \cos \psi} \int_0^\eta V d\eta + \frac{1}{W_e} \frac{\partial W_e}{\partial \psi} \int_0^\eta V d\eta \\ + \frac{1}{W_e} \frac{\partial W_e}{\partial s} \frac{1}{1+\alpha \cos \psi} \int_0^\eta W d\eta . \end{aligned} \quad (2.3.54)$$

In particular, the radial velocity at the outer edge of the boundary layer is found by setting $\eta = \delta(\psi, s_o)$, where $\delta(\psi, s_o)$ is the conventional boundary layer thickness. To convert the integrals in equation (2.3.54) to the M.I.R. notations, we notice that

$$\int_0^{\eta=\delta(\psi, s_o)} \frac{\partial W}{\partial s} d\eta = \frac{\partial}{\partial s} \int_0^\delta W d\eta - \frac{\partial \delta}{\partial s} = \frac{\partial}{\partial s} \int_0^1 W Z dW - \frac{\partial \delta}{\partial s} .$$

However,

$$\delta = \int_0^1 Z dW$$

from equation (2.3.52); thus, one has

$$\int_0^\delta \frac{\partial W}{\partial s} d\eta = \frac{\partial}{\partial s} \int_0^1 (W-1) Z dW . \quad (2.3.55)$$

Substituting equation (2.3.55) into (2.3.54), we obtain

$$\begin{aligned} U_e = \int_0^1 \frac{\partial V}{\partial \psi} Z dW - \frac{1}{1+\alpha \cos \psi} \frac{\partial}{\partial s} \int_0^1 (1-W) Z dW - \left(\frac{\alpha \sin \psi}{1+\alpha \cos \psi} - \frac{1}{W_e} \frac{\partial W_e}{\partial \psi} \right) \int_0^1 V Z dW \\ + \frac{1}{W_e} \frac{\partial W_e}{\partial s} \frac{1}{1+\alpha \cos \psi} \int_0^1 W Z dW , \end{aligned} \quad (2.3.56)$$

where U_e is the outer edge normal velocity component. Rewriting U_e in the outer variable notation, we have

$$U_o = \frac{W_o}{D^{\frac{1}{2}}} U_e . \quad (2.3.57)$$

In summary, we have obtained expressions for the boundary layer velocity components and the displacement thickness from the corresponding solution of Z and V . We shall now proceed to discuss the coupled solution of the inviscid region and the viscous region.

Interaction between the core and the boundary layer regions

Initially, the boundary layer equations are integrated using the two-dimensional point vortex as the outer solution. The displacement thickness and the outer edge normal velocity are calculated respectively from equations (2.3.49) and (2.3.56). The velocity potential in the core region is then recalculated using the normal velocity as the boundary condition at $r_o=1$, instead of at the outer edge, provided the displacement

thickness is thin enough. The necessary outer velocity components and their gradients in the azimuthal and streamwise directions are calculated at $r_0 = 1$ from the core potential. Again, assuming the boundary layer is thin compared to the radius of the pipe cross-section, these velocity components and gradients are used as conditions at the outer edge of the boundary layer for the next integration of the boundary layer equations. The process is repeated until there is no appreciable change in the results between successive iterations.

The crucial assumption here is that the boundary layer must be thin enough so that the region of the core flow is essentially the same as the interior of the curved pipe. Since the boundary layer thickness is of order $O(D^{-\frac{1}{2}})$, this assumption is reasonable for large Dean number. The assumption fails, of course, when separation occurs. Furthermore, the present iteration scheme is generally applicable to weak interaction situations, which means the boundary layer must be relatively thin.

2.4 Results and discussion for the entry curved pipe flow

Numerical results have been obtained for the whole flow field inside a 90° elbow for various values of the curvature ratio and Reynolds number. The core region and the boundary layer are coupled together through the simple interaction scheme described before. Results converge usually after thirty iterations.

The overall accuracy of the present model is restricted by the accuracy of the boundary layer calculation. The integration of the integral relations is done by a variable order Adams-Moulton method, which requires fewer derivative evaluations than the commonly used Runge-Kutta method. Nevertheless, the main computing effort is spent on the boundary layer equations. For example, with $N=1$ in the M.I.R. formulation (i.e., first approximation), the computing time for the integration of the reduced boundary layer equations (consisting of 10 ordinary differential equations) requires about twice as much time as for the core region, which needs about 1 second on a CDC 7600 machine. Since the computation time increases rather rapidly as the order of approximation for integral relations increases, we are contented with the second approximation in the present analysis. It is believed that the second approximation provides accurate prediction of the flow behavior, and also requires little computer time (about 5 minutes for 40 iterations).

During the iteration process, it is necessary to relax the outer edge radial velocity in order to achieve convergence within a reasonable number of iterations. The following simple relaxation scheme has been employed:

$$U_o^{v(\text{new})} = U_o^{v-1} + \omega(U_o^v - U_o^{v-1}) \quad , \quad 0 < \omega < 1 \quad , \quad (2.4.1)$$

where U_o^v and U_o^{v-1} are the outer edge normal velocity (equation (2.3.57)) evaluated from the current (v th) boundary layer calculation and the previous ($v-1$)th boundary layer calculation, respectively. $U_o^{v(\text{new})}$ is the relaxed outer edge normal velocity for the calculation of the v th core flow. The ($v-1$)th normal velocity is then updated by setting it equal to $U_o^{v(\text{new})}$:

$$U_o^{v-1} = U_o^{v(\text{new})} \quad . \quad (2.4.2)$$

The correct choice of w is very important in the present scheme and is discussed in Appendix C.

Finally, we mention that the initial station, z_i , has been chosen as 0.0025 in the present investigation. One can then calculate the values of $\{b_{kl}, k=0,1,\dots,N-1\}$ at this particular z_i from equation (2.3.40). Other values of z_i have been used ($z_i = 0.005$, $z_i = 0.0075$) and the results of the boundary layer equations do not differ much from each other, within the accuracy of the integration scheme.

Figure 9 shows the displacement thickness (equation (2.3.49)) along the curved pipe at different azimuthal locations. The streamwise variable is modified as $\tilde{s} = \phi/\pi/2$. It is relatively thin compared with the radius of the pipe, except at the inner bend, $\psi = 180^\circ$, where it increases continuously as the flow moves downstream as one would expect physically. The variation of the displacement thickness azimuthally is shown in Fig. 10. At the early stage of the flow, the boundary layer is thinner at the inner bend than it is at the outer bend. This is because initially the outer flow is faster at the inner bend than at the outer bend (potential vortex profile) and the curvature effect is small. As the flow develops, the curvature effect becomes dominant and the boundary layer is thicker at the inner bend than at the outer bend. Further

downstream, the boundary layer stays quite uniform around the pipe and increases abruptly when $\psi = 180^\circ$ is approached. This indicates secondary flow separation somewhere ahead of $\psi = 180^\circ$.

Next, the variation of the average azimuthal velocity, \bar{V}^\ddagger , along the pipe and around the pipe are shown in Figs. 11 and 12, respectively. The absolute magnitude of the azimuthal velocity inside the boundary layer is small everywhere, as indicated in the figures. It is interesting to note that \bar{V} attains its maximum first at about $\psi = 60^\circ$. This maximum location then shifts towards 90° and remains near there as the flow develops further downstream. Finally, typical profiles of the axial velocity and azimuthal velocity across the boundary layer are shown in Fig. 13 at a particular location.

We now turn to the flow in the core region. The development of the secondary flow at different streamwise sections is shown in Fig. 14. The cross flow velocity vector at each node is drawn. The direction of the flow is represented by the direction of the arrow and the magnitude by the arrow's length. Very near the entry, the cross flow behavior is the same as that predicated by the pure inviscid analysis (section 2.2), thus justifying the assertion that the viscous effect is minimal near the entry. Here the secondary motion is directed from the outer bend ($\psi < 90^\circ$) towards the inner bend ($\psi > 90^\circ$), as shown in Fig. 14(a). Physically, since the flow develops from a uniform profile to the potential vortex profile immediately downstream of the entry section, the fluid must move from the outer bend to the inner bend for reasons of mass conservation requirement. As the flow develops, the secondary motion begins to reverse its direction and, in Fig. 14(c), the fluid has already moved from the inner bend towards the outer bend. This is, of course, due to the boundary layer growth around the pipe cross section.

[‡]The average azimuthal velocity is defined as $\bar{V} = \int_0^1 V dW$.

This secondary motion persists further downstream to the exit. It is important to realize that the cross flow is indeed very small compared to the axial motion, as indicated by the velocity scales used in Fig. 14. Furthermore, the direction of the cross flow is essentially parallel to the plane of symmetry at all the stations shown in Fig. 14, an assumption which has been used by many other investigators of the curved pipe flow.

The axial velocity profiles at three parallel planes, as shown in Fig. 15(f), are drawn in Figs. 15(a)-(e). Since the boundary layer in the present study is very thin, except near $\psi = 180^\circ$ when the flow develops further downstream, the axial velocity profile does not change much over the entire elbow. Thus, the characteristic of the potential vortex profile is seen at every station shown in Fig. 15. The velocity is higher at the inner bend than it is at the outer bend. Furthermore, the velocity results are almost independent of the vertical distance measured from the symmetry plane. For the last station, Fig. 15(d), the axial velocity results at the inner symmetry plane ($\psi = 180^\circ$) may not be valid because the boundary layer there is relatively thick. Instead, we have indicated the boundary layer axial velocity profile there. The present model does not predict the shift of the maximum axial velocity towards the outer bend. This is not surprising because we have assumed that the viscous region is confined near the pipe wall everywhere. As the viscous region at the inner bend extends further into the core region, the fluid is pushed towards the outer bend, thereby causing the maximum axial velocity shift. For flow at low to moderate Reynolds number, this maximum shift occurs shortly downstream of the entry section. For flow at high Reynolds number, as in the present study, the viscous region at the inner bend is relatively small over a much longer distance in the entry region. As a result, the shift and the

maximum velocity occur much later. Of course, the shift occurs first at the symmetry plane for all Reynolds number. Finally, the results show that the core flow is accelerated, only slightly, due to the displacement effect.

In summary, we have obtained numerical results for the entry curved pipe flow, both in the boundary layer and in the core region. The assumption of a potential core is consistent with the experimental results of Agrawal, Talbot and Gong near the entry of the pipe. Further downstream, the strong interaction between the core and the boundary layer near the vicinity of $\psi = 180^\circ$ may render the irrotational assumption invalid. Moreover, the boundary layer may well be turbulent near the exit region and the present analysis will not apply.

III. PARTICLE PHASE

3.0 Some fundamentals of the particulate phase in a gas solid mixture

Having discussed in great detail the motion of the gas phase, we now consider the particulate phase. As mentioned in Chapter I, relatively few investigations have been made for a three-dimensional gas-particle flow system. The general theory of multiphase fluid dynamics is very complicated when every aspect of the interaction between different phases is considered.

The main difficulty in solving gas-particle flows, or any other two phase systems for that matter, is due to the momentum (and possibly energy) coupling of the fluid and the solid phases which makes it necessary to solve simultaneously the governing equations for both phases. This is further complicated by such phenomena as particle-particle interaction, attrition of particles due to collisions with the system boundary and with other particles, reflection or deposition on the pipe wall, just to name a few. The equations of motion for the particulate phase are not yet well established when such phenomena are accounted for.

There exist two major methods to formulate the particle phase in a dilute suspension: the Lagrangian description and the Eulerian description. The Lagrangian description fixes attention on a single particle throughout its whole trajectory in the region of interest. The Eulerian formulation, on the other hand, assumes the particle phase as a continuum and the resulting governing equations for the particle phase are quite similar to the well-known Navier-Stokes equations in fluid mechanics. As described, the Lagrangian formulation is on a microscopic scale, and particle-particle collision must be accounted for even in a dilute suspension. Nevertheless, one can apply some sort of statistical average to

the individual particle equation of motion and thus obtain the trajectories (or streamlines) of the mean particle motion. The important point here is to realize that the results only represent the macroscopic behavior of the particle motion, but not the microscopic behavior of each individual particle. To this extent, the effect of averaging the Lagrangian equation of motion is equivalent to replacing the convective derivatives in the Eulerian equation of motion by the corresponding material (or total) derivative, in the usual terminology of continuum mechanics.

In the present analysis, we shall confine ourselves to obtaining particle trajectories, up to the first impact point with the wall, in a dilute suspension in which particle-particle interaction can be neglected. The Lagrangian equations of motion are employed, since they are most suitable to obtaining particle trajectories. It must be understood that only the macroscopic behavior of the particle phase is of interest here. Since the particle trajectories are obtained up to the first impact point, no boundary condition for the particle phase is needed.

3.1 Equations of motion for the two phase system

In addition to the assumption of a dilute suspension, the following assumptions are made:

(1) The presence of particles does not affect the gas flow field. Strictly speaking, this is not an additional assumption because it only holds when the suspension is dilute. We shall discuss this further.

(2) We shall only consider the aerodynamic drag force exerted by the fluid phase on the particle phase due to differences in velocity of the two phases. Other forces, such as gravity force, pressure force, etc., are assumed to be insignificant. Furthermore, we assume that the drag force is given by Stokes law throughout the region of interest.

(3) When particles first hit the pipe wall, they are assumed to be stuck there without reflecting back into the carrier fluid. This assumption excludes the fact that particles reflecting from the wall may collide with the oncoming particles, with a much larger likelihood, and thus alter their original paths.

(4) The transport properties of the mixture are approximated by those of the fluid phase alone.

(5) The static pressure of the dilute suspension is due solely to the fluid phase. This is justified since the R.M.S. speed of the particles is very much less than that of the gas molecules.

By virtue of assumption (2), the momentum equation for the gas phase can be written as, in vector notation,

$$\vec{v}_f \vec{\nabla} \vec{v}_f = \nu_f \nabla^2 \vec{v}_f - \frac{1}{\rho_f} \vec{\nabla} p + \frac{\rho_p}{\rho_f} \frac{\vec{v}_p - \vec{v}_f}{\tau_m}, \quad (3.1.1)$$

where \vec{v} is the velocity vector, ν the kinematic viscosity, ρ the phase density in the mixture and τ_m is the momentum equilibration time.

Subscripts f and p refer to the fluid and the particle, respectively.

In the regime of Stokes law, τ_m is given by

$$\tau_m = \frac{2}{9} \frac{\sigma^2 \bar{\rho}_p}{\mu_f}, \quad (3.1.2)$$

where $\bar{\rho}_p$ denotes the material density of the particle, σ the particle diameter and μ_f the viscosity of the fluid phase. From equation (3.1.1), the last term on the right-hand side represents the momentum coupling between the fluid and the particles. Thus, for a dilute suspension, the phase density of the particles is very small compared with that of the fluid and one can neglect the coupling term for a first order approximation. On the other hand, if the momentum equilibration time, τ_m , is very small, one would have a situation that the particles adjust their motion to the fluid motion very fast and their relative velocity ($\vec{v}_p - \vec{v}_f$) will vanish practically, in which case the coupling term is again negligible.

Without the coupling term, equation (3.1.1) reduces to the usual Navier-Stokes equation for a single phase system. Hence, the results of Chapter II can be used to calculate the particle trajectories. In effect, we neglect terms of order β or higher, where β is given by

$$\beta = \frac{\rho_p}{\rho_f}, \quad (3.1.3)$$

as is easily seen from equation (3.1.1). As mentioned before, when τ_m is very small, the relative velocity ($\vec{v}_p - \vec{v}_f$) will also be very small so that the parameter β is again the small parameter in equation (3.1.1). Indeed, it can be shown that the relative velocity is of order $\tilde{L}_m = \frac{W_i \tau_m}{L}$, where W_i and L are the characteristic velocity and length of the flow system (Yeung, 1978). A question remaining is that for particles with large τ_m , it appears that one can neglect the coupling term in (3.1.1) even though the density of particle phase, ρ_p , is comparable to ρ_f .

However, if $\rho_p \sim \rho_f$, one would have a nondilute suspension and equation (3.1.1) would not hold anyway.

For the particle phase, we shall use the cylindrical polar coordinate system (r, z, ϕ) as shown in Fig. 16. Denoting the velocity components in the increasing r, z and ϕ direction by u, v and w , respectively, the Lagrangian equations of motion are

$$\frac{du_p}{d\bar{t}} = \frac{w_p^2}{\bar{r}} + \frac{u_f - u_p}{\tilde{L}_m}, \quad (3.1.4)$$

$$\frac{dw_p}{d\bar{t}} = -\frac{u_p w_p}{\bar{r}} + \frac{w_f - w_p}{\tilde{L}_m}, \quad (3.1.5)$$

$$\frac{dv_p}{d\bar{t}} = \frac{v_f - v_p}{\tilde{L}_m}, \quad (3.1.6)$$

$$\frac{d\bar{r}}{d\bar{t}} = u_p, \quad (3.1.7)$$

$$\frac{d\phi}{d\bar{t}} = \frac{w_p}{\bar{r}}, \quad (3.1.8)$$

$$\frac{dz}{d\bar{t}} = \frac{v_p}{\alpha}, \quad (3.1.9)$$

where the velocity components are referred to the constant entry speed W_i , \bar{r} to the mean radius of curvature R , \bar{z} to the radius of the pipe, a , and \bar{t} to the characteristic time R/W_i . α is the familiar curvature ratio and \tilde{L}_m is defined as

$$\tilde{L}_m = \frac{W_i \tau_m}{R}.$$

The initial conditions are given as

$$\left. \begin{aligned} w_p &= 1, & u_p &= v_p = 0 \\ \bar{r} &= \bar{r}_0, & \bar{z} &= \bar{z}_0, & \phi &= 0 \end{aligned} \right\} \text{ at } \bar{t} = 0. \quad (3.1.10)$$

With the fluid flow field known from section 2.4, equations (3.1.4) to (3.1.9) can be integrated simultaneously to give the particle trajectories. The continuity equation is satisfied by requiring that the density of particles along each particle trajectory be constant. In this particular situation, one can simplify the integration by assuming the following:

(1) Since the boundary layer is relatively thin, the particle velocity at the outer edge of the boundary will be essentially the same as that at the wall. Thus, one can ignore the presence of the viscous layer when computing the particle trajectories. This assumption does not apply to those particles that are initially inside the boundary layer, i.e., particles near the wall.

(2) The secondary motion of the gas can be neglected compared with its axial motion, as indicated by the results of the last chapter. Furthermore, since the axial velocity profile of the gas essentially corresponds to the potential vortex profile, we shall assume that w_f is given by the following:

$$w_f = \frac{C}{r}, \quad (3.1.11)$$

where C is an average constant determined from the axial velocity results at different streamwise stations.

The above two assumptions fail when the boundary layer is relatively thick. As indicated in section 2.4, the velocity profile at the symmetry plane near the exit region is quite different from the vortex profile. Fortunately, in many practical situations, most particles hit the pipe wall long before the exit region is reached. In these cases, equation

(3.1.11) should be adequate. With the help of these two assumptions, equations (3.1.4) to (3.1.9) become

$$\frac{du_p}{dt} = \frac{w_p^2}{r} - \frac{u_p}{\tilde{L}_m} , \quad (3.1.12)$$

$$\frac{dw_p}{dt} = - \frac{u_p w_p}{r} + \frac{C/r - w_p}{\tilde{L}_m} , \quad (3.1.13)$$

$$\frac{dr}{dt} = u_p , \quad (3.1.14)$$

$$\frac{d\phi}{dt} = \frac{w_p}{r} , \quad (3.1.15)$$

and

$$v_p = 0 , \quad \bar{z} = z_0 , \quad \forall \bar{t} . \quad (3.1.16)$$

3.2 Particle trajectories and density distribution along the pipe wall

Equations (3.1.12) to (3.1.15) are integrated, using initial conditions (3.1.10), up to the first impact point. For systems having small values of \tilde{L}_m ($\tilde{L}_m < 1$), there exist matched asymptotic expansion solutions (Yeung, 1978). In the limit where $\tilde{L}_m \rightarrow 0$, the particle motion and the gas motion become identical with each other. Indeed, it can be readily shown that the particle velocity and trajectory are given by

$$\begin{aligned} u_p &= 0, \quad w_p = \frac{C}{\bar{r}_0}, \\ \bar{r} &= \bar{r}_0, \quad \phi = \frac{C}{\bar{r}_0^2} \bar{t}. \end{aligned} \quad (3.2.1)$$

Notice that w_p does not satisfy the initial condition imposed on the particle phase. This is solely due to the assumption made on the gas motion (equation (3.1.11)) which neglects the very small region over which the uniform entry profile transforms to the potential vortex profile.

On the other hand, when \tilde{L}_m assumes a very large value, the effect of the gas motion on the particle is negligible. In such cases, the particles experience essentially no drag force and will maintain their initial motion until they hit the pipe wall. When the drag force terms in equations (3.1.12) and (3.1.13) are neglected, one can obtain closed form solutions for the unknowns. They are given by

$$\begin{aligned} u_p &= \frac{\bar{t}}{\sqrt{\bar{t}^2 + \bar{r}_0^2}}, \quad w_p = \bar{r}_0 \sqrt{\frac{1}{\bar{t}^2 + \bar{r}_0^2}}, \\ \bar{r} &= \sqrt{\bar{t}^2 + \bar{r}_0^2}, \quad \phi = \tan^{-1} \frac{\bar{t}}{\bar{r}_0}. \end{aligned} \quad (3.2.2)$$

The particle trajectories in this case are simply straight lines normal to the entry plane.

Having obtained the particle trajectories and velocity components, we can calculate the density of the particle phase at the pipe wall from the continuity equation. To do this, we consider a stream tube around a particular trajectory as shown in Fig. 17. Point A denotes the impact location. The impact velocity q and the impingement angle, θ , measured from the tangent of the pipe surface are given by

$$q(A) = \sqrt{u_p^2(A) + w_p^2(A)} \quad , \quad (3.2.3)$$

$$\theta(A) = \tan^{-1} \frac{u_p(A)}{w_p(A)} \quad . \quad (3.2.4)$$

Denoting the area intercepted by this stream tube on the pipe wall by Σ , we can relate the density at point A by equating the mass flow rate of particles at the entry plane and at Σ :

$$\rho_p(A) = \frac{M_o}{u_p(A)\Sigma} \quad , \quad (3.2.5)$$

where M_o is the initial mass flow rate of particles across the area intercepted by the stream tube at the entry plane. In the special case where $\tilde{L}_m \rightarrow 0$, (3.2.5) is not applicable since Σ is undefined. Indeed, one must consider the boundary layer region in order to predict the particle density at the wall in this case. On the other hand, if $\tilde{L}_m \rightarrow \infty$, one obtains from (3.2.2) the impact normal velocity as

$$u_p(A) = \sin \phi \quad . \quad (3.2.6)$$

Also, the area Σ can be related to the area at the initial plane, denoted by A_o , by the following

$$A_o = \Sigma \sin \phi \quad . \quad (3.2.7)$$

Substituting (3.2.6) and (3.2.7) into (3.2.5), we obtain the particle

density at the wall as

$$\rho_p(A) = \rho_{p_0} \quad , \quad (3.2.8)$$

where ρ_{p_0} is the entry particle density and is assumed constant in the present analysis.

3.3 Results and Discussion

Results for the particle trajectories and density distribution have been obtained for a curved pipe with $\alpha = 0.1$. Figure 18 shows the particle trajectories for different values of \tilde{L}_m at the plane $\bar{z} = 0.1$. The constant C in equation (3.1.11) has been found to be

$$C = 1.05 \quad (3.3.1)$$

from the results obtained in section 2.4. It is interesting to observe that the particle trajectories are essentially straight lines for \tilde{L}_m as low as 3. This indicates that the asymptotic solution obtained in section 3.2 for $\tilde{L}_m \rightarrow \infty$ has a much wider range of validity than is expected mathematically. As \tilde{L}_m decreases, the particle trajectories are bent more and more toward the streamlines of the gas flow field, which is, of course, expected physically. When \tilde{L}_m is less than 0.1, some particles leave the pipe without making any impact with the outer wall. In the limit, as $\tilde{L}_m \rightarrow 0$, one would expect that most particles leave the pipe without hitting the wall. It is worthwhile to notice that the asymptotic solution for $\tilde{L}_m \rightarrow 0$ gives poor results even for \tilde{L}_m as small as 0.1. In this sense, it has a much smaller range of applicability compared with the solution for $\tilde{L}_m \rightarrow \infty$.

Figure 19(a) shows the area at the outer bend that is intercepted by the particles that originate from the initial plane. The lines $\bar{r}_0 = \text{constant}$ in this diagram represent the impact locations of those particles that originate at the specified radial coordinate, r_0 . Only the outer bend is impinged by the particles under the assumptions made in this analysis. In the actual case, particles reflected from the outer bend would impinge on the inner bend further downstream of the first

impact area.

The density distribution of the particles at the pipe wall is calculated from equation (3.2.5). The area Σ is calculated in the following way: The entry plane is divided into a rectangular grid system as shown in Fig. 19(b). Consider the square ABCD. The stream tube initiated from this square will intercept the outer wall at A'B'C'D', as shown in Fig. 19(a). The area of the curvilinear rectangle A'B'C'D' is Σ . The normal velocity of impingement at the center of A'B'C'D' is approximated by the average of the normal velocity at A', B', C' and D'.

Figure 20 shows the density distribution along the pipe wall in the streamwise direction for two values of \tilde{L}_m . Consistent with the results for the trajectories, the particles are concentrated at the entry region for large \tilde{L}_m and spread out further to the exit region as \tilde{L}_m decreases. The density distribution is quite uniform in both cases. We have also indicated the actual numerical values of the particle density obtained by the use of Figs. 19(a) and (b) for $\tilde{L}_m = 0.5$. Since the area Σ is evaluated roughly by counting the squares in Fig. 19(a), the numerical results scatter about the mean value 1.0 as shown in Fig. 20. The increase in ρ_p for $\tilde{L}_m = 0.1$ may be due to the diminishing normal velocity $u_p(A)$ in that case. Finally, we plot the density distribution, angle of impingement and impact velocity in Fig. 21 for the case in which $\tilde{L}_m = 0.5$. Such plots supply important information for the calculation of, say, the relative erosion rate per unit area of the pipe wall.

The discussion made in this section is based solely on the present numerical results. It has been shown that the results obtained are physically reasonable although we have used many simplifying assumptions for the particle phase. The validity of these results should increase for large \tilde{L}_m since in that case, the particle motion is only slightly

affected by the gas motion. Consequently, any approximation made regarding the gas flow field does not induce significant error to the results of the particle motion.

IV. CONCLUSIONS

The fluid dynamics of a gas-particle mixture in the entry region of a circular curved pipe have been investigated and numerical results have been obtained for a curved pipe with $\alpha = 0.1$ and Reynolds number $R_e = 10^4$. Other values of $\alpha(0.05)$ and $R_e(10^5)$ have been tried and the results obtained are all qualitatively the same. Much of the emphasis has been placed on the numerical solution of the gas phase. The numerical schemes used in the present study are quite different from other theoretical investigations of the same topic. An efficient scheme has been devised, based on the conventional Telenin's method, to solve the Laplace equation in three dimensions. The orthonormal method of integral relations has been applied successively to obtain numerical solution to the present three-dimensional boundary layer equations.

Results of the fluid flow field conform with the recent measurement of Agrawal, Talbot and Gong. By taking into account the interaction with the boundary layer, it has been shown that there is a novel reversal of the direction of the secondary motion in the core region. For the boundary layer region, the present results agree qualitatively with those obtained by Yao and Berger (1974). In particular, the secondary motion inside the viscous layer is always from the outer to the inner bend. This conforms with the fact that the boundary layer acts as a reservoir receiving fluid in the outer bend and losing it in the inner bend. On the other hand, the boundary layer is thin except near the proximity of $\psi = 180^\circ$, where there is a relatively large outflow from the boundary layer. Direct quantitative comparison is not possible because of the different methods of attack and the different range of Reynolds number considered.

As for the particle phase, a first order solution for the particle trajectories has been obtained. Simplifying assumptions have been made which render the two phases uncoupled from each other. In this respect, only simple particle dynamics is involved in the present analytical work. Indeed, the method of solution for the particle phase is similar to the author's previous investigation regarding the erosion in a curved pipe (Yeung, 1977). The only difference is the form of the gas velocity profile. In view of these assumptions, no more than a qualitative validity can be claimed for these results, particularly regarding the density of particles at the pipe wall.

REFERENCES

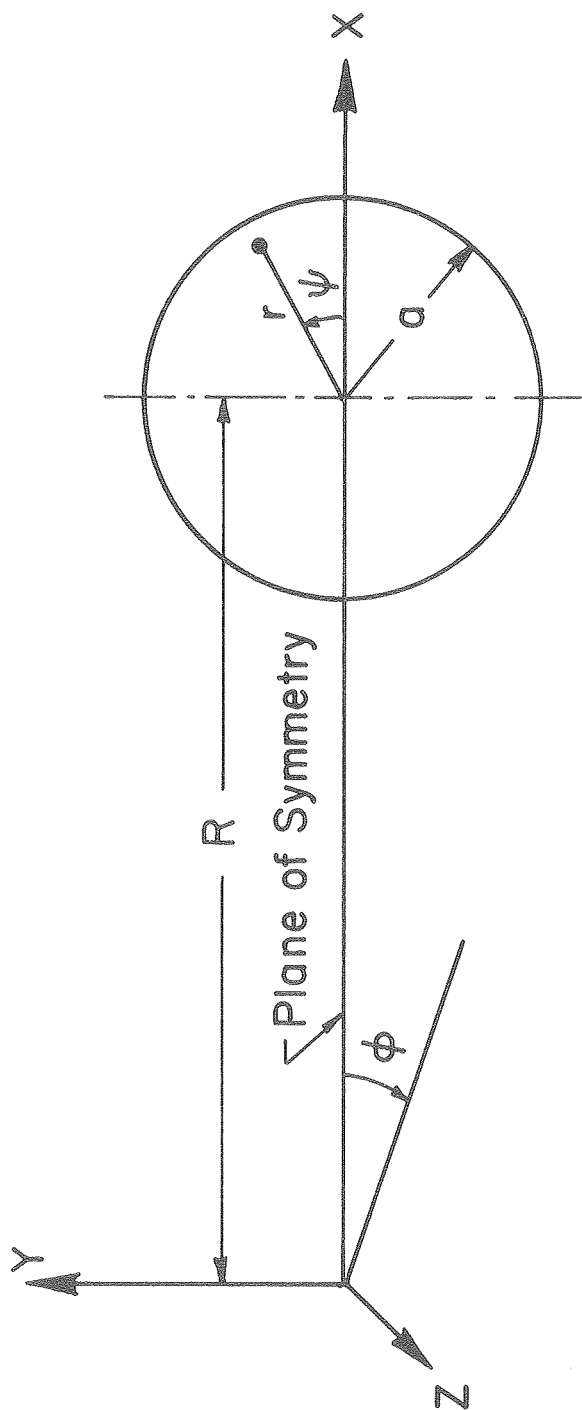
- Abbott, D. E., and Bethel, H. E. Application of the Galerkin-Kantorovich-Dorodnitsyn Method of Integral Relations to the Solution of Steady Boundary Layers. *Ingenieur-Archiv.* 37, No. 2 (1968).
- Agrawal, Y., Talbot, L., and Gong, K. Laser Anemometry Study of Entry Curved Pipe Flow. *J. Fluid Mech.* 85, part 3 (1978).
- Barua, S. N. On Secondary Flow in Stationary Curved Pipes. *Quart. J. Mech. Appl. Math.* XVI, part 1 (1963).
- Choi, U. S. Experimental Study of Wall Shear Rates in the Entry Region of a Curved Tube. Ph.D. Thesis, University of California, Berkeley, 1978.
- Collins, W. M., and Dennis, S. C. R. The Steady Motion of a Viscous Fluid in a Curved Tube. *Quart. J. Mech. Appl. Math.* 28 (1975).
- Dean, W. R. Note on the Motion of Fluid in a Curved Pipe. *Phil. Mag.* 4 (1927).
- Dean, W. R. The Streamline Motion of Fluid in a Curved Pipe. *Phil. Mag.* S7 5, No. 30 (1928).
- Dorodnitsyn, A. A. Solution of Mathematical and Logical Problems on High-Speed Digital Computers. *Proc. Conf. Develop. Soviet Mach. Machines and Devices, Part 1*, 44-52, VINITI Moscow (1956).
- Dorodnitsyn, A. A. *Advances in Aeronautical Sciences*, Vol. 3. New York, Pergamon Press (1960).
- Fletcher, C. A. J., and Holt, M. Modified Version of the Method of Integral Relations. *J. Computational Physics* 18 (1975).
- Fletcher, C. A. J., and Holt, M. Supersonic Flow over Cones at Large Angles of Attach. *J. Fluid Mech.* 74 (1976).
- Garabedian, P. R. *Partial Differential Equations*. Wiley (1964).
- Gilbert, M., Allport, J., and Dunlap, R. Dynamics of Two-Phase Flow in Rocket Nozzles. *ARS Journal* (Dec. 1962).
- Gilinskii, S. M., Telenin, G. F., and Tinyakov, G. P. *Izv. Akad. Nauk. SSSR Mekh. Mash.* 4 (1964) (translated as NASA TTF297).
- Greenspan, D. Secondary Flow in a Curved Pipe. *J. Fluid Mech.* 57, part 1 (1973).
- Hawthorne, W. R. Secondary Circulation in Fluid Flow. *Proc. Roy. Soc.* A 206 (1951).

- Holt, M. Numerical Methods in Fluid Dynamics. Springer-Verlag, Berlin, Heidelberg, New York (1977).
- Ito, H. Laminar Flow in Curved Pipes. ZAMM 49, part 11 (1969).
- Isaacson, E., and Keller, H. B. Analysis of Numerical Methods, p. 199. Wiley (1966).
- Kliegel, J. R. Gas Particle Nozzle Flows. Ninth Symp. (Intl.) on Combustion (1963). Academic Press.
- Lyne, W. H. Unsteady Viscous Flow in a Curved Pipe. J. Fluid Mech. 45, part 1 (1970).
- McConalogue, D. J., and Srivastava, R. S. Motion of a Fluid in a Curved Tube. Proc. Roy. Soc. A 307 (1968).
- Modarress, D. Application of the Method of Integral Relations to Boundary Layer Flows over Blunt Bodies. Computer Methods in Appl. Mech. and Eng. 14, No. 2 (1978).
- Rudinger, G. Gas-Particle Flow in Convergent Nozzles at High Loading Ratios. AIAA 8, No. 7 (1970).
- Smith, F. T. Steady Motion Within a Curved Pipe. Proc. Roy. Soc. A 347 (1976a).
- Smith, F. T. Fluid Flow into a Curved Pipe. Proc. Roy. Soc. A 351 (1976b).
- Singh, M. P. Entry Flow in a Curved Pipe. J. Fluid Mech. 65 (1974).
- Singleton, R. E. The Compressible Gas-Solid Particle Flow over a Semi-Infinite Flat Plate. ZAMM 16 (1965).
- Soo, S. L. Laminar and Separated Flow of a Particulate Suspension. Astronautica Acta 11 (1965).
- Soo, S. L. Non-Equilibrium Fluid Dynamics—Laminar Flow over a Flat Plate. ZAMP 19 (1968).
- Soo, S. L., and Tung, S. K. Deposition and Entrainment in Pipe Flow of a Suspension. Powder Technology 6, No. 5 (1972).
- Soo, S. L., and Tung, S. K. Pipe Flow of Suspensions in Turbulent Fluid—Electrostatic and Gravity Effects. Appl. Sci. Res. 24 (1971).
- Van Dyke, M. Perturbation Methods in Fluid Mechanics. Parabolic Press (1975).

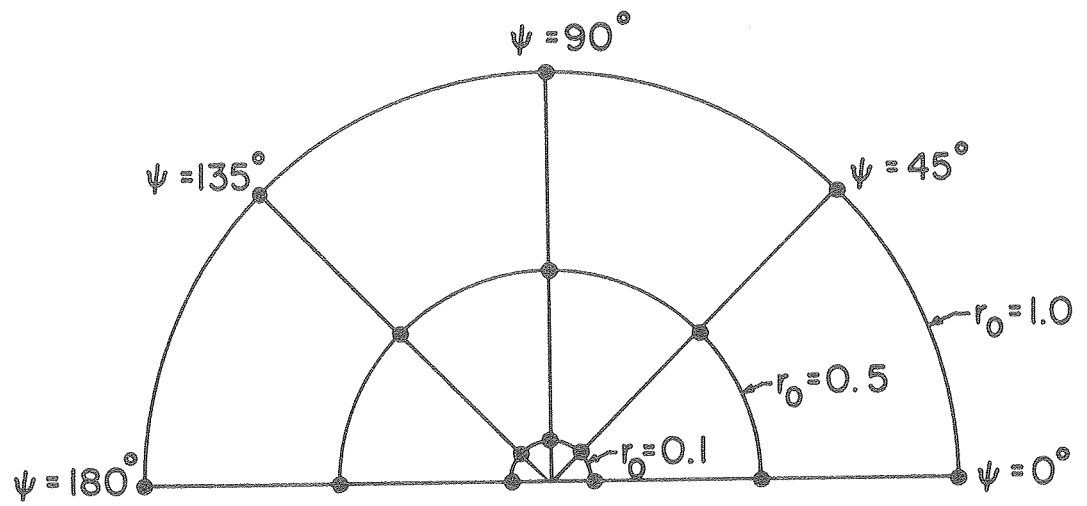
Yao, L. S., and Berger, S. A. Entry Flow in a Curved Pipe. J. Fluid Mech. 67, part 1 (1975).

Yeung, W. S. Erosion in a Curved Pipe: Wear (to appear 1979).

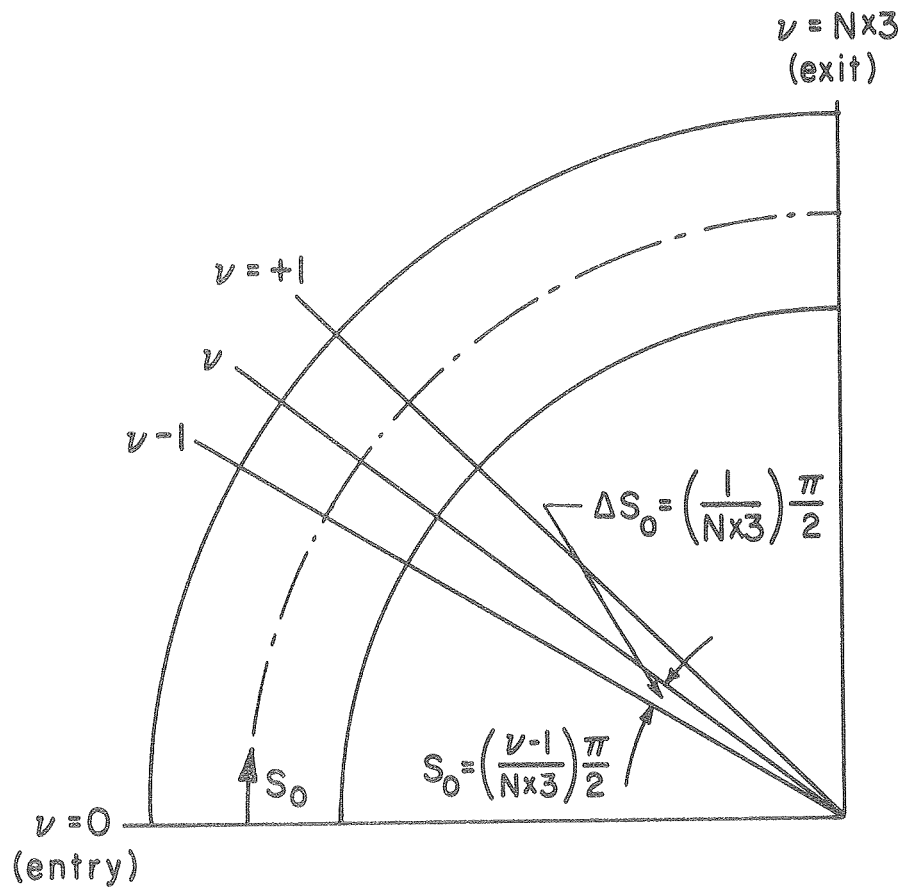
Yeung, W. S. Perturbation Solutions for the Particle Trajectories of a Gas-Solid Mixture Entering a Curved Duct. Lawrence Berkeley Laboratory, Berkeley, Calif., Report #8521.



XBL 795-6207



XBL795-6208



XBL 795-62 09

$$\frac{\partial^2 \Omega}{\partial r^2} + \frac{1}{r} \frac{\partial \Omega}{\partial r} + \frac{1}{r^2} \frac{\partial^2 \Omega}{\partial \phi^2} + \frac{\partial^2 \Omega}{\partial z^2} = 0$$

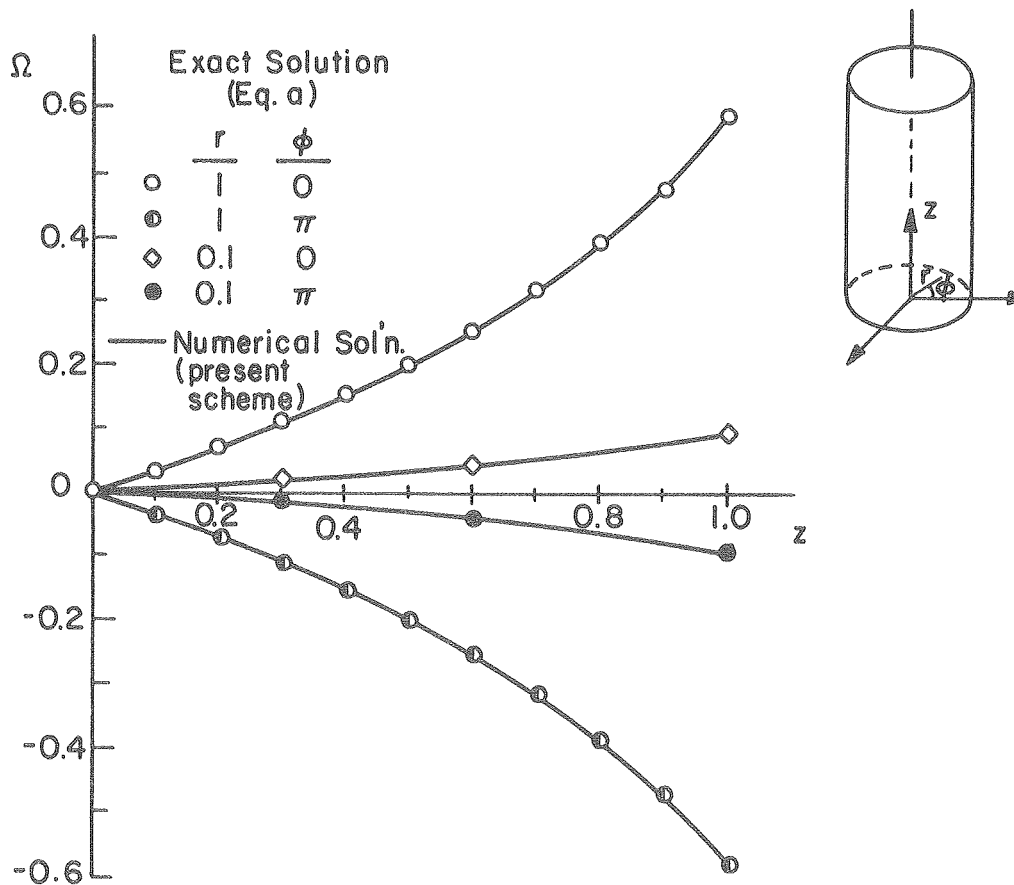
$$0 < r < 1, \quad 0 < \phi < \pi, \quad 0 < z < 1$$

$$\text{B.C.} \quad \frac{\partial \Omega}{\partial r} = 0, \quad r = 1, \quad \frac{\partial \Omega}{\partial z} = \frac{\alpha \cos \phi J_1(\alpha r)}{\sinh \alpha}, \quad z = 0$$

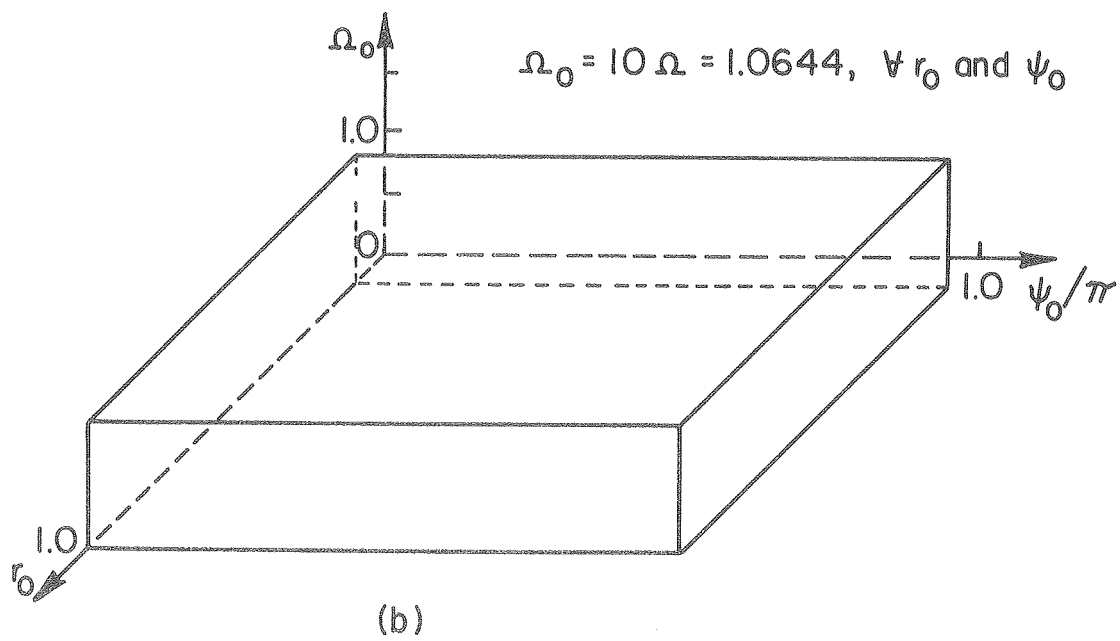
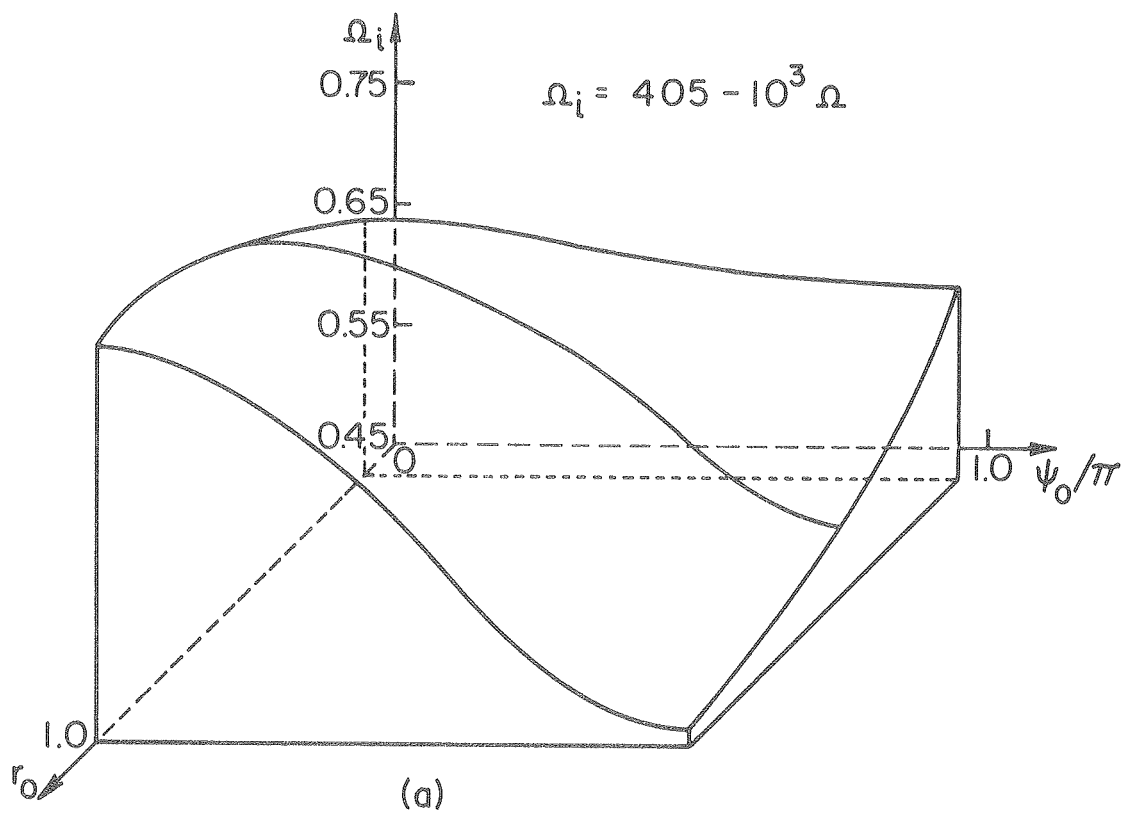
$$\frac{\partial \Omega}{\partial z} = \frac{\alpha \cos \phi J_1(\alpha r) \cosh \alpha}{\sinh \alpha}, \quad z = 1, \quad \alpha = 1.8412$$

$$\text{Exact solution:} \quad \Omega = \frac{J_1(\alpha r) \cos \phi \sinh \alpha z}{\sinh \alpha}$$

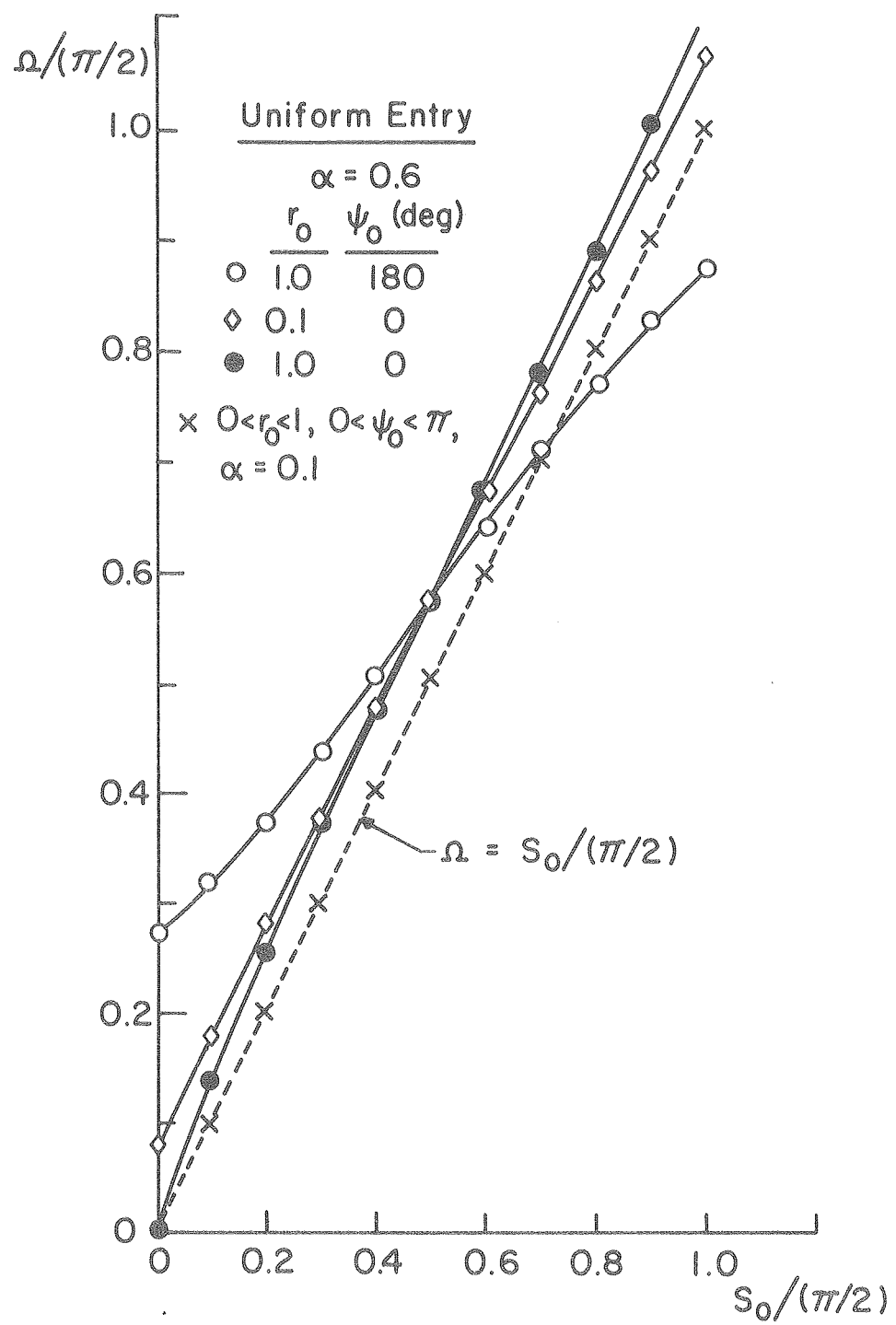
$$\text{Numerical:} \quad \Omega \cong \sum_{j=1}^3 \Omega_j^o r^{2j-1}, \quad \Omega \cong \sum_{j=1}^3 \Omega_j^{oo} \cos(j-1)\phi$$



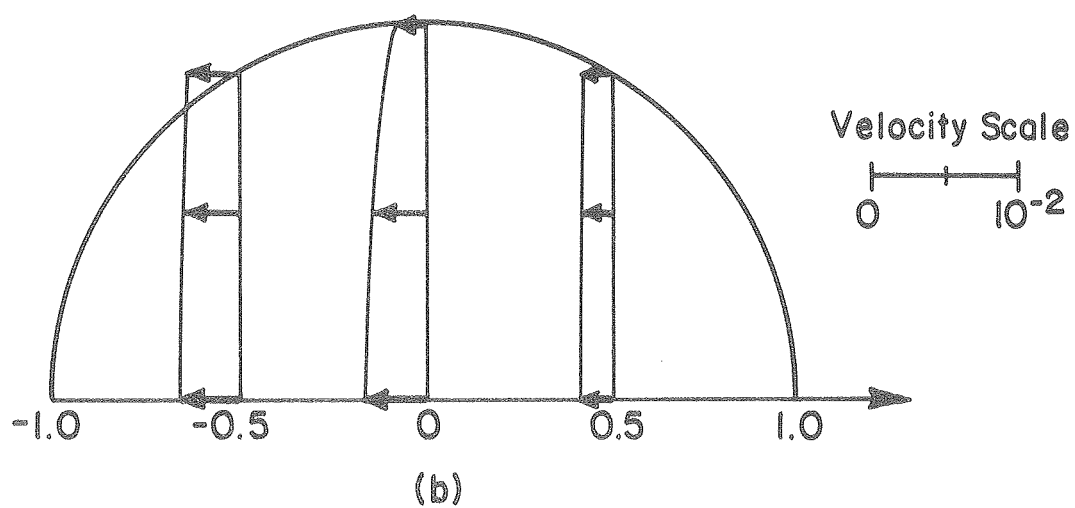
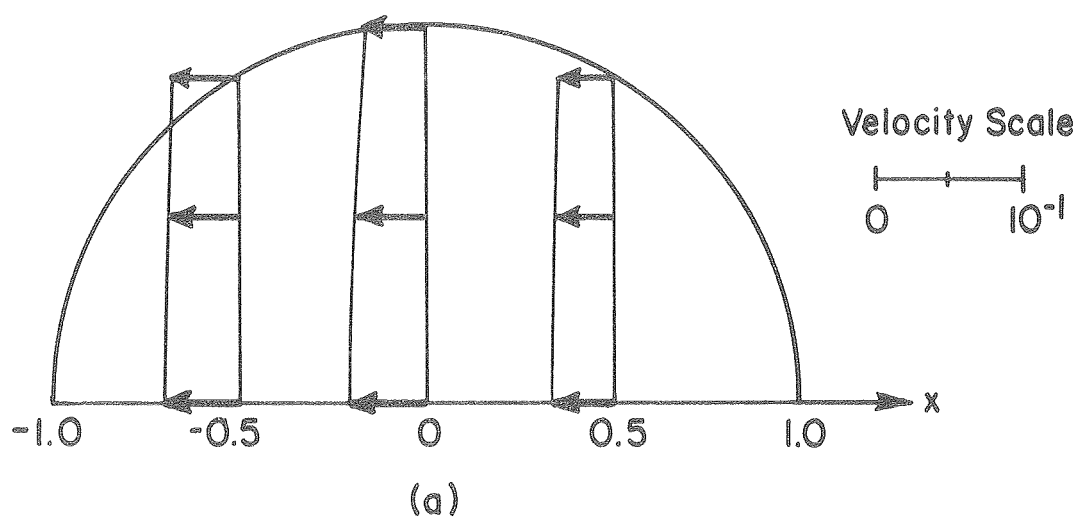
XBL 795-6210



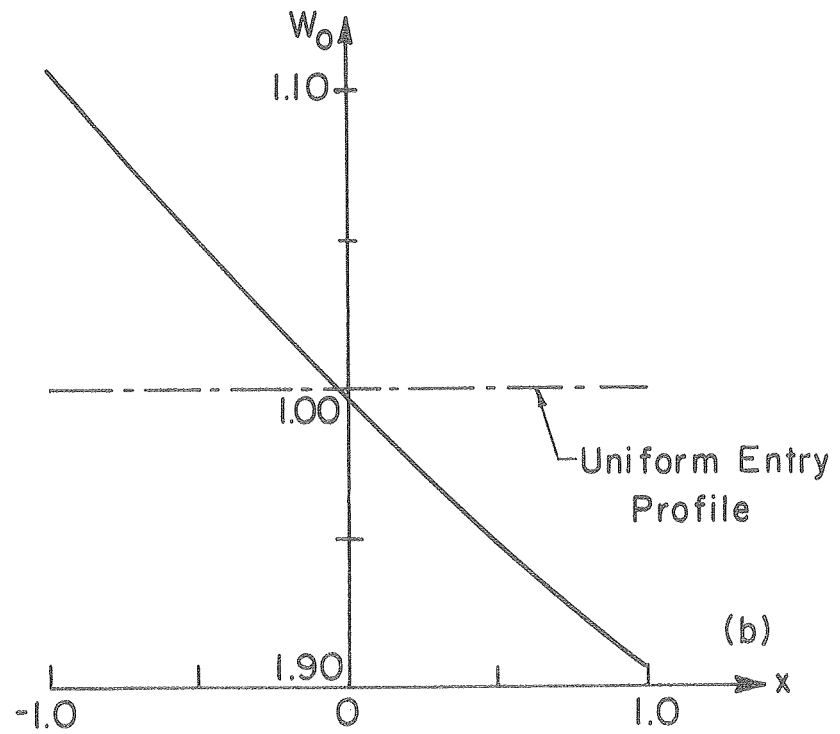
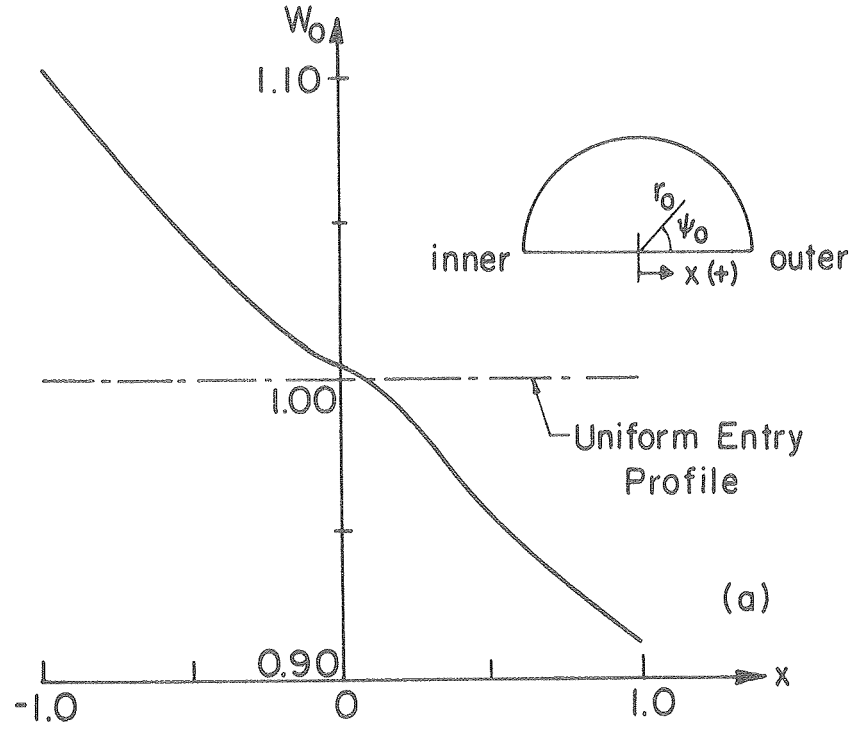
XBL 795-6211

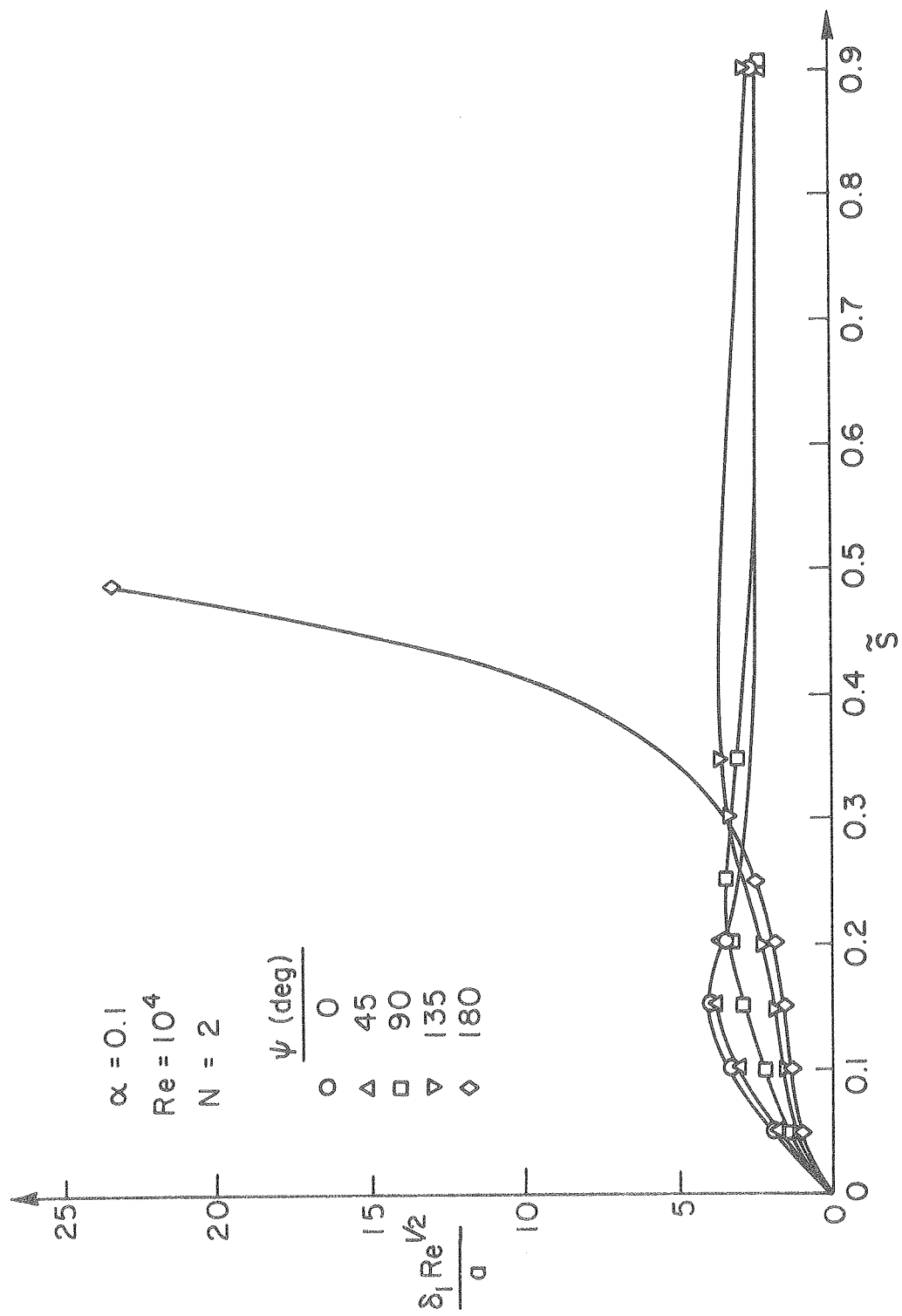


XBL 795-6212

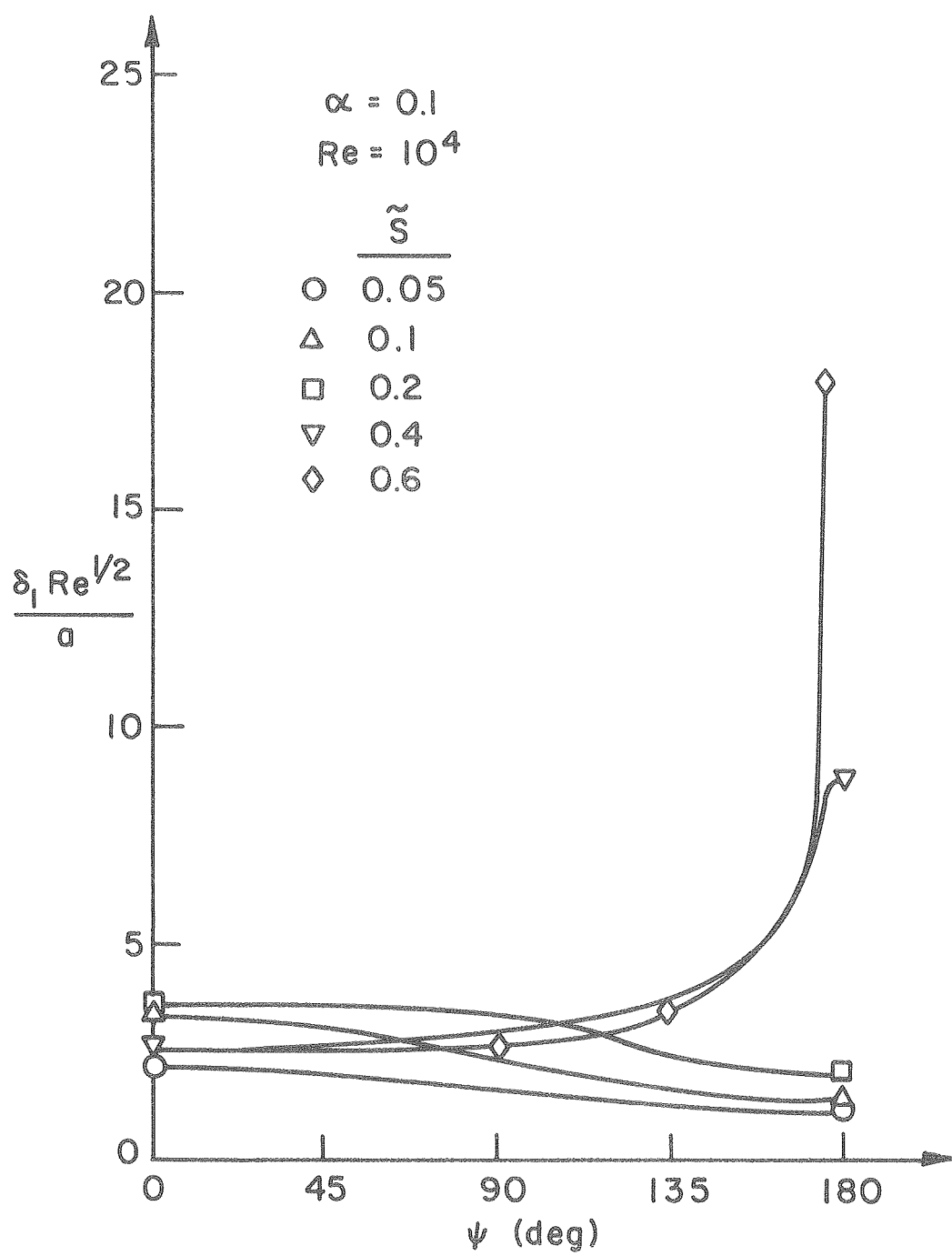


XBL795-6213

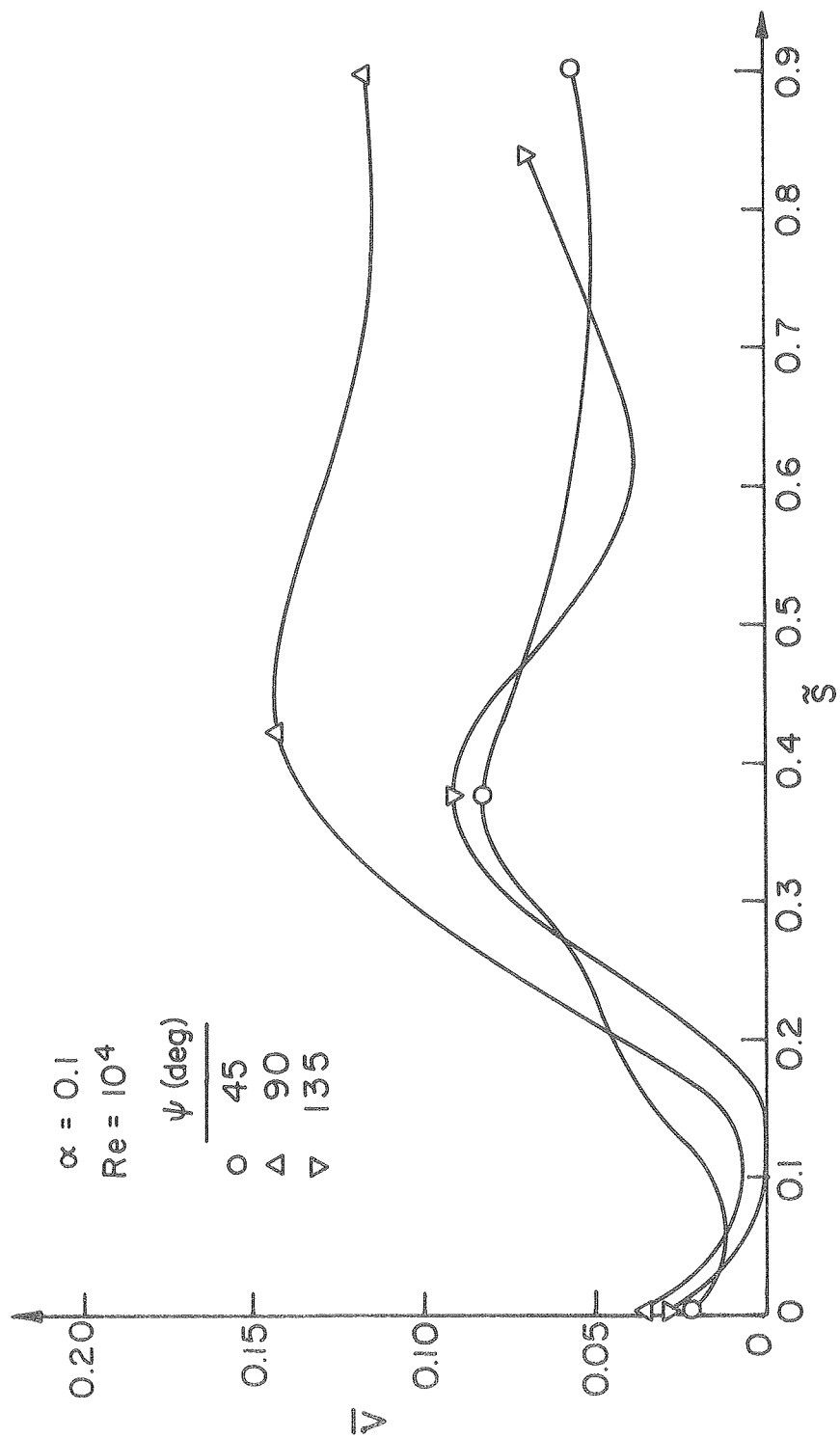




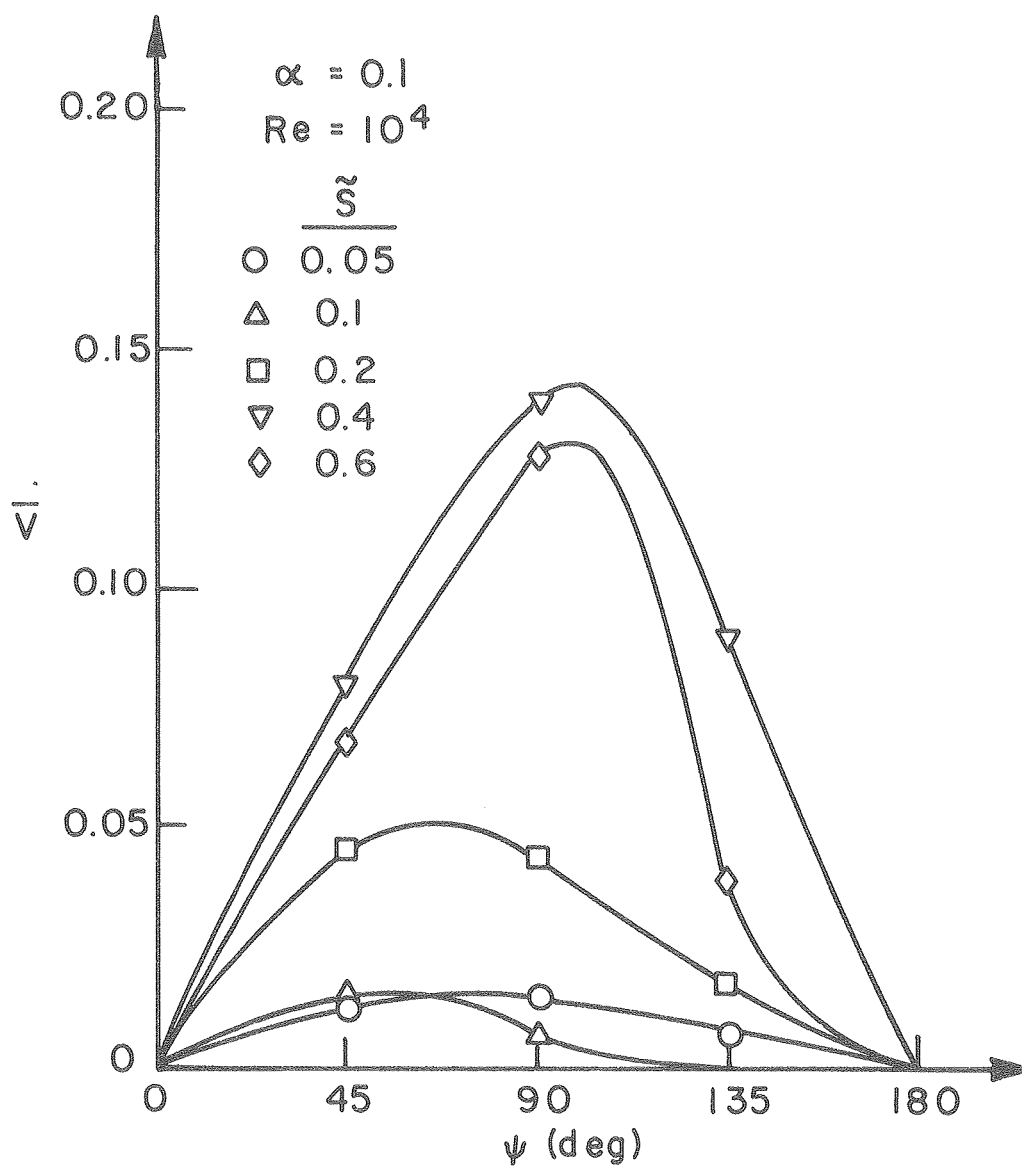
XBL 795-6215



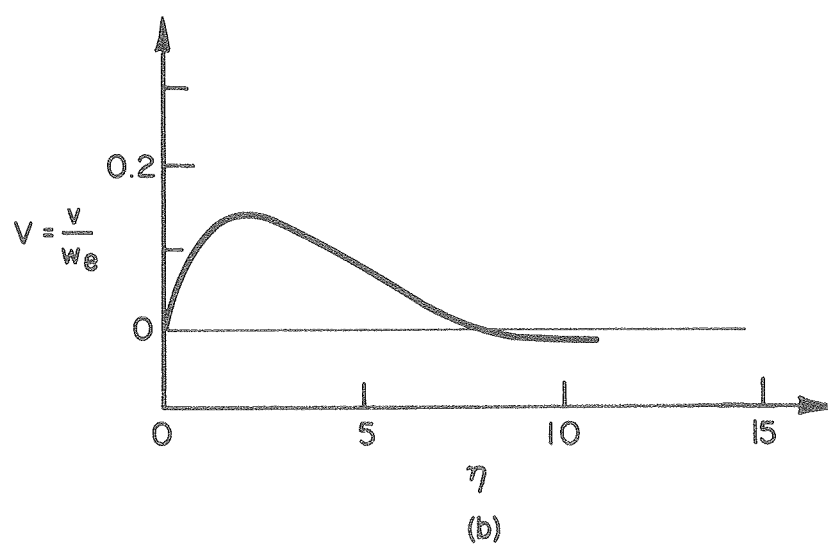
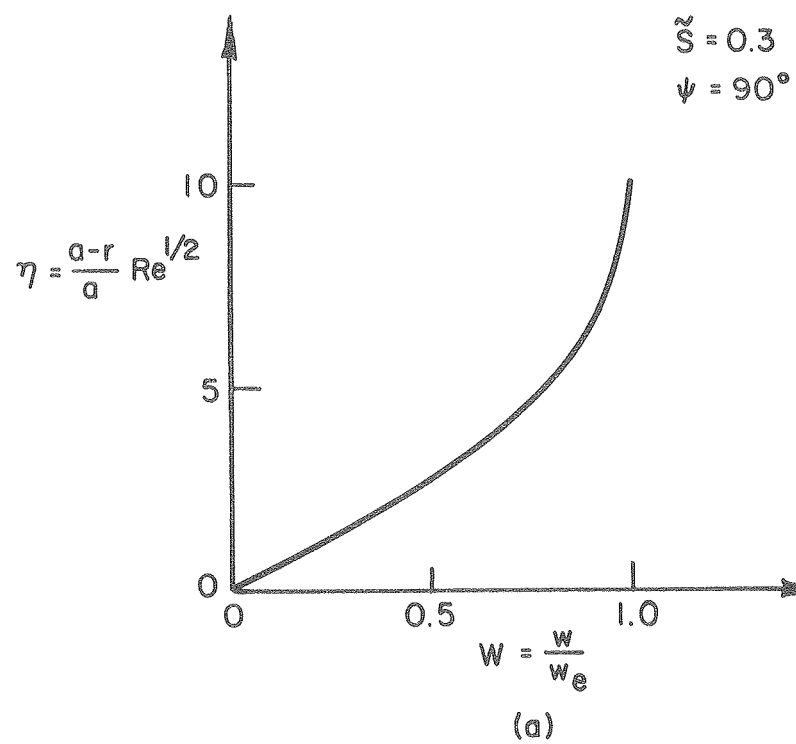
XBL 795-6216



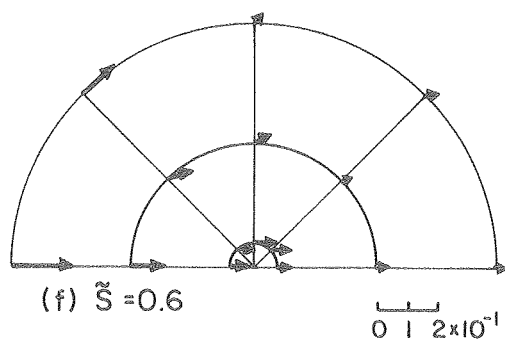
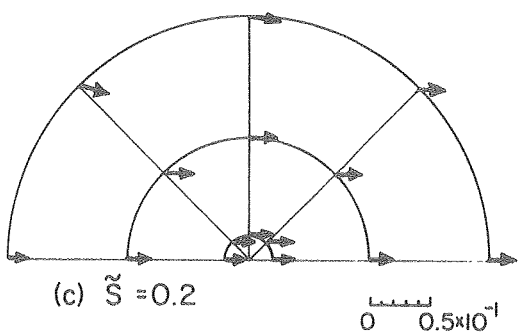
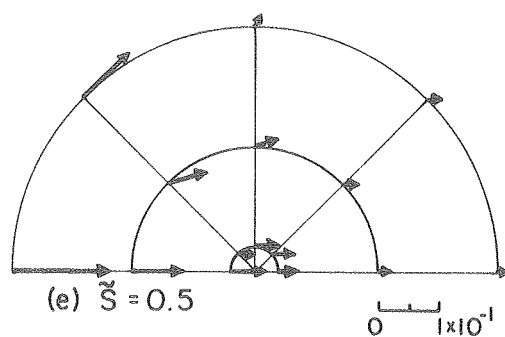
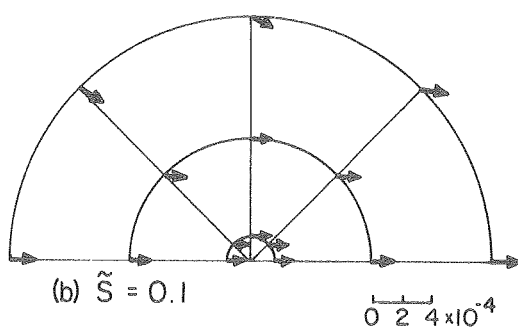
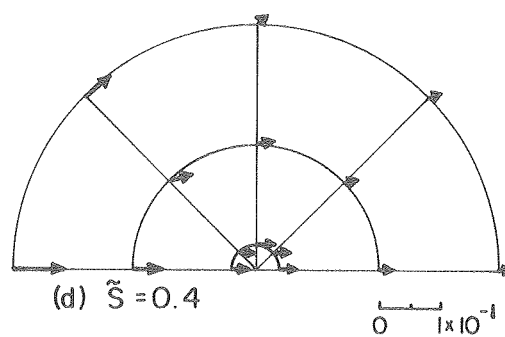
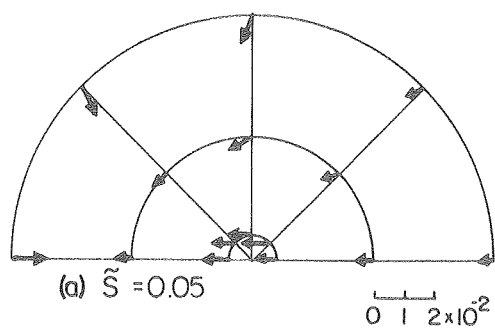
XBL 795-6217



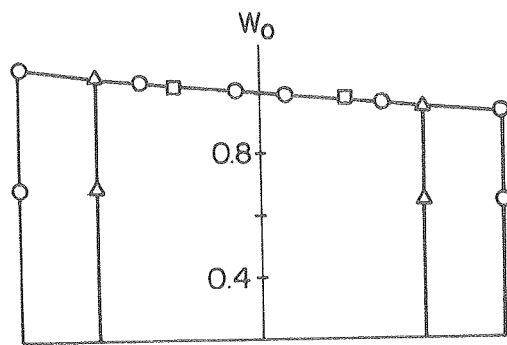
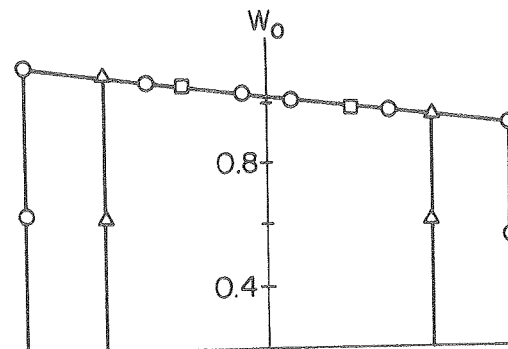
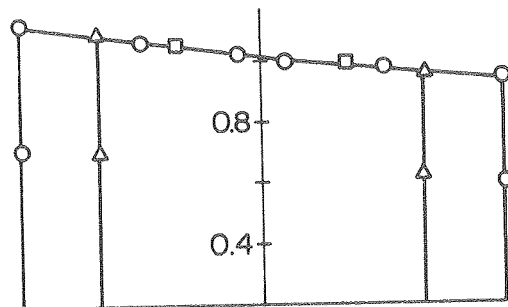
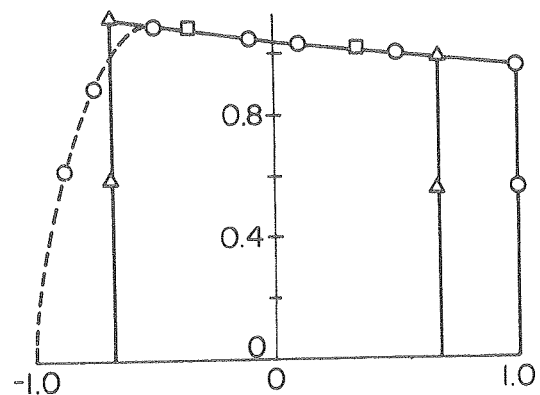
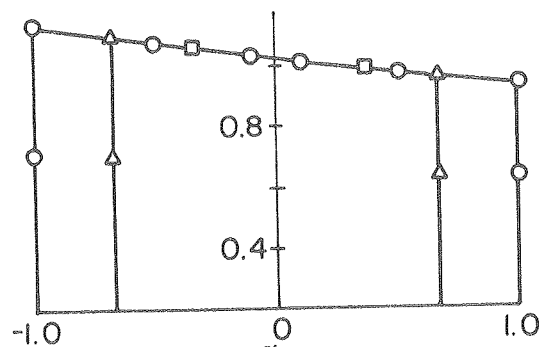
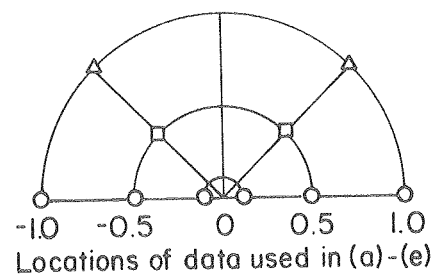
XBL 795-6218



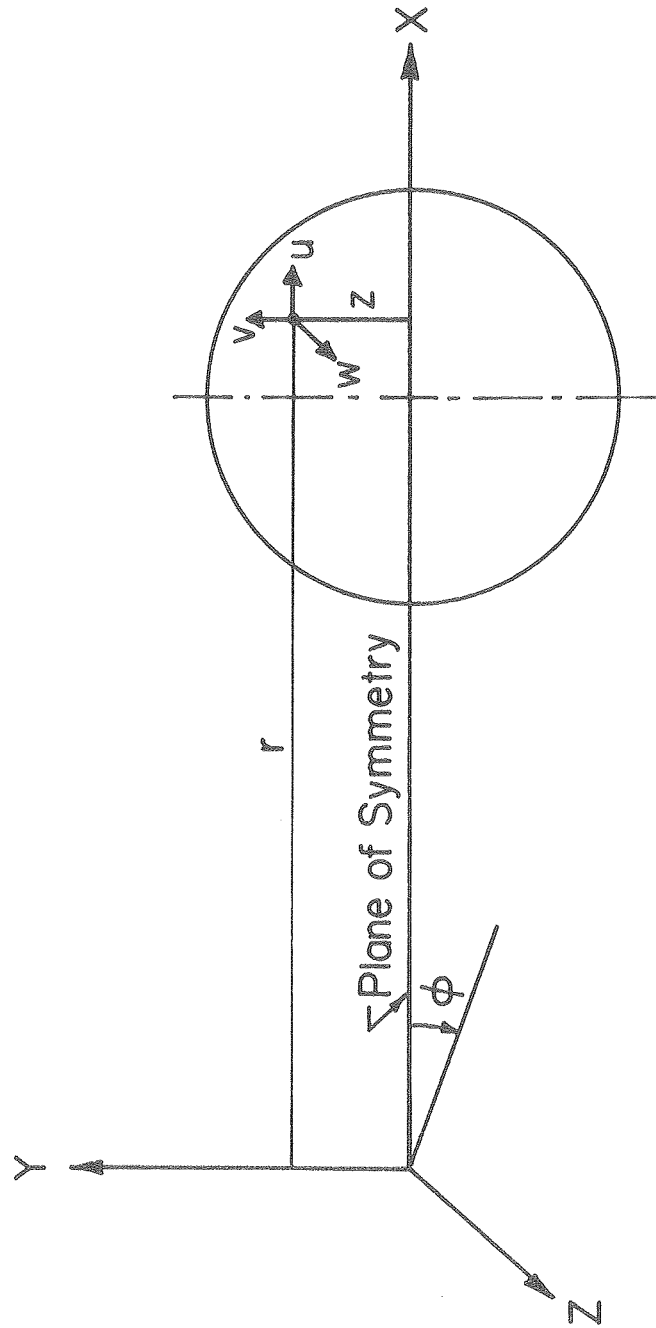
XBL 795-6219



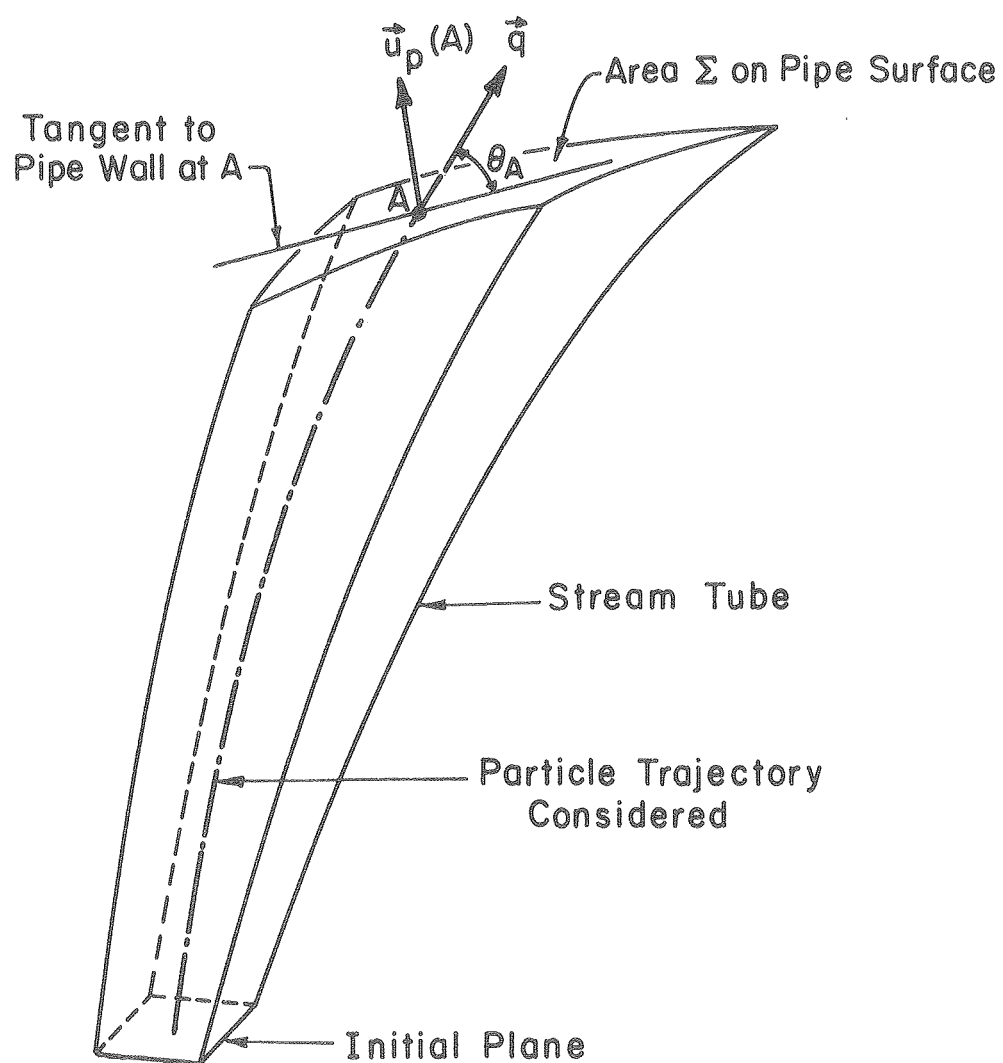
XBL795-6220

(a) $\tilde{S} = 0.05$ (d) $\tilde{S} = 0.3$ (b) $\tilde{S} = 0.1$ (e) $\tilde{S} = 0.5$ (c) $\tilde{S} = 0.2$ 

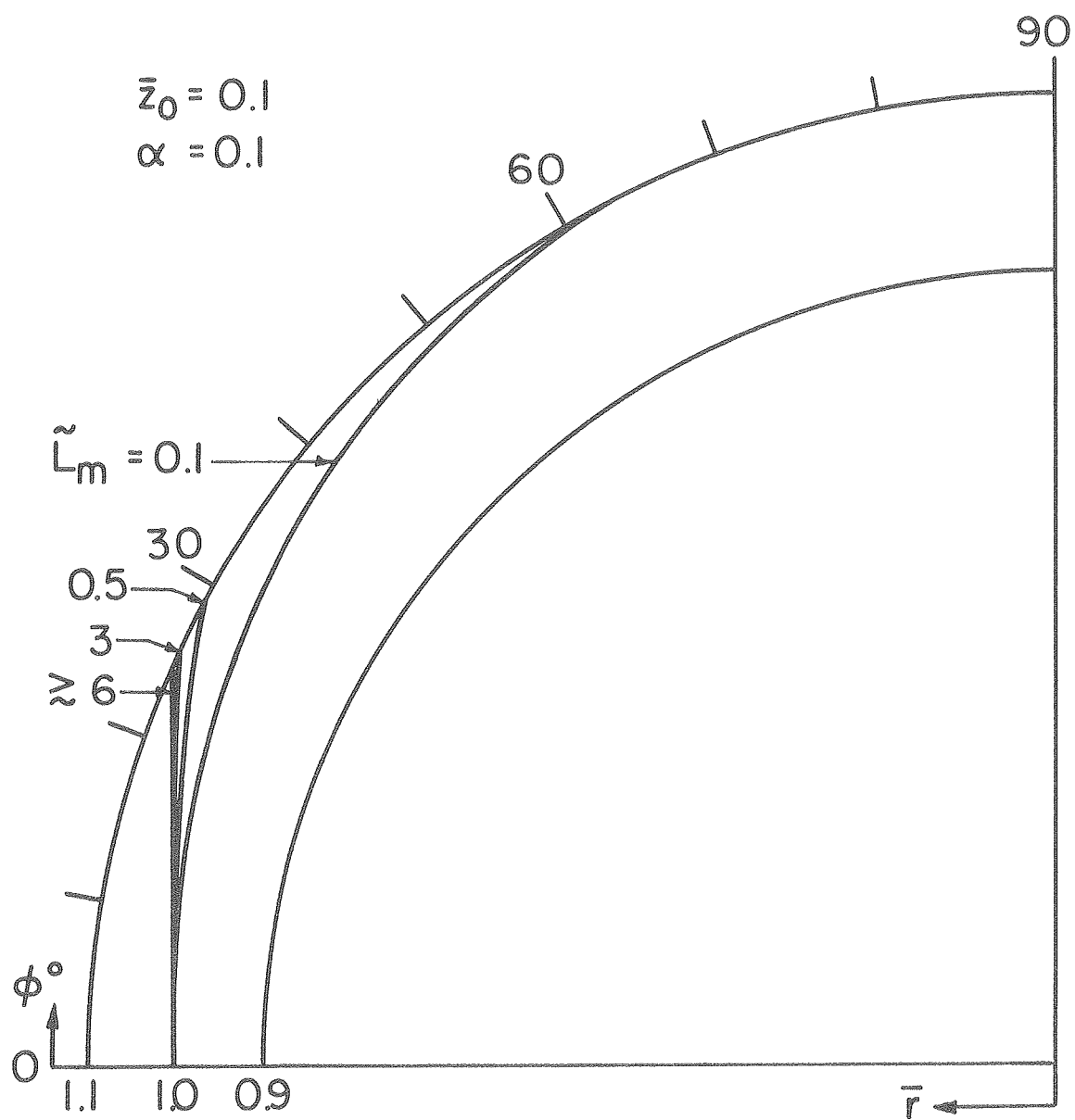
XBL795-6221



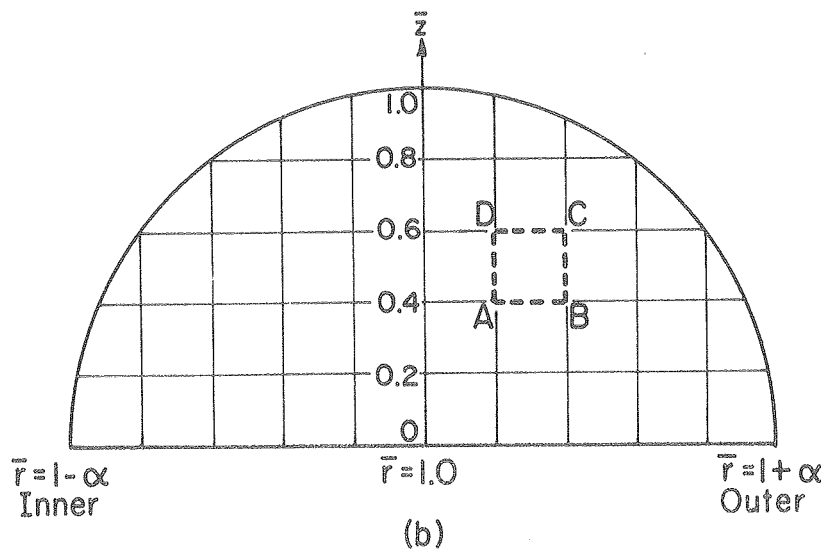
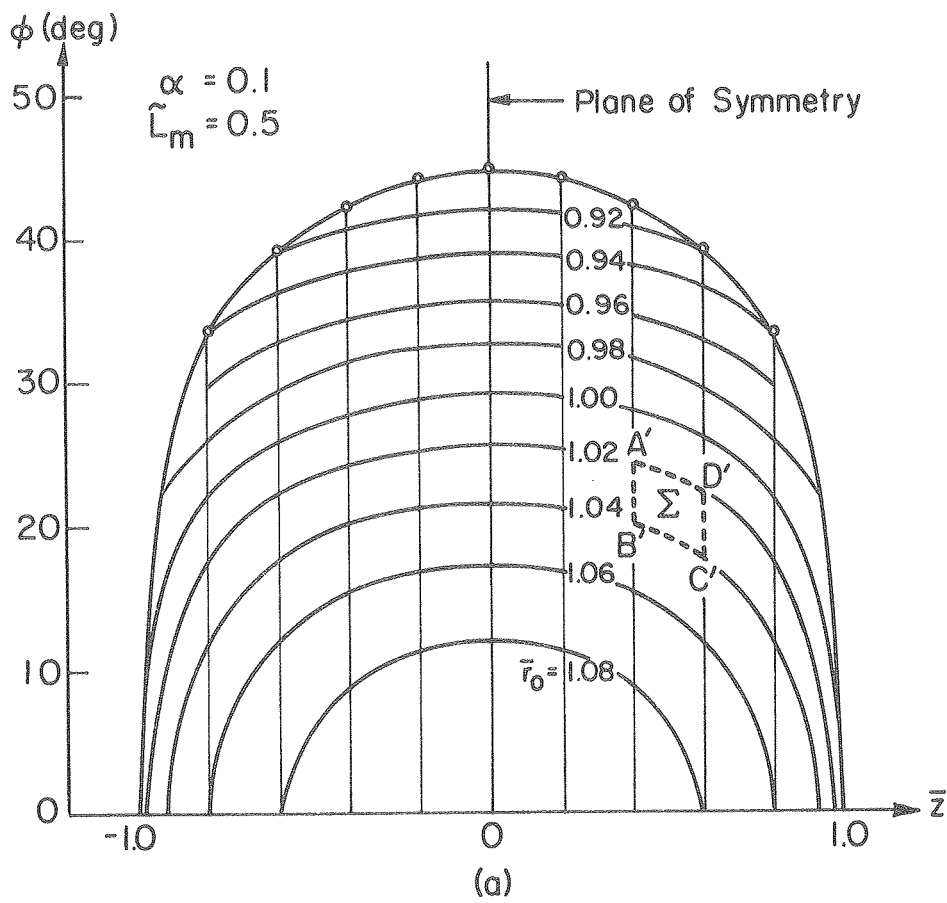
XBL 795-6222



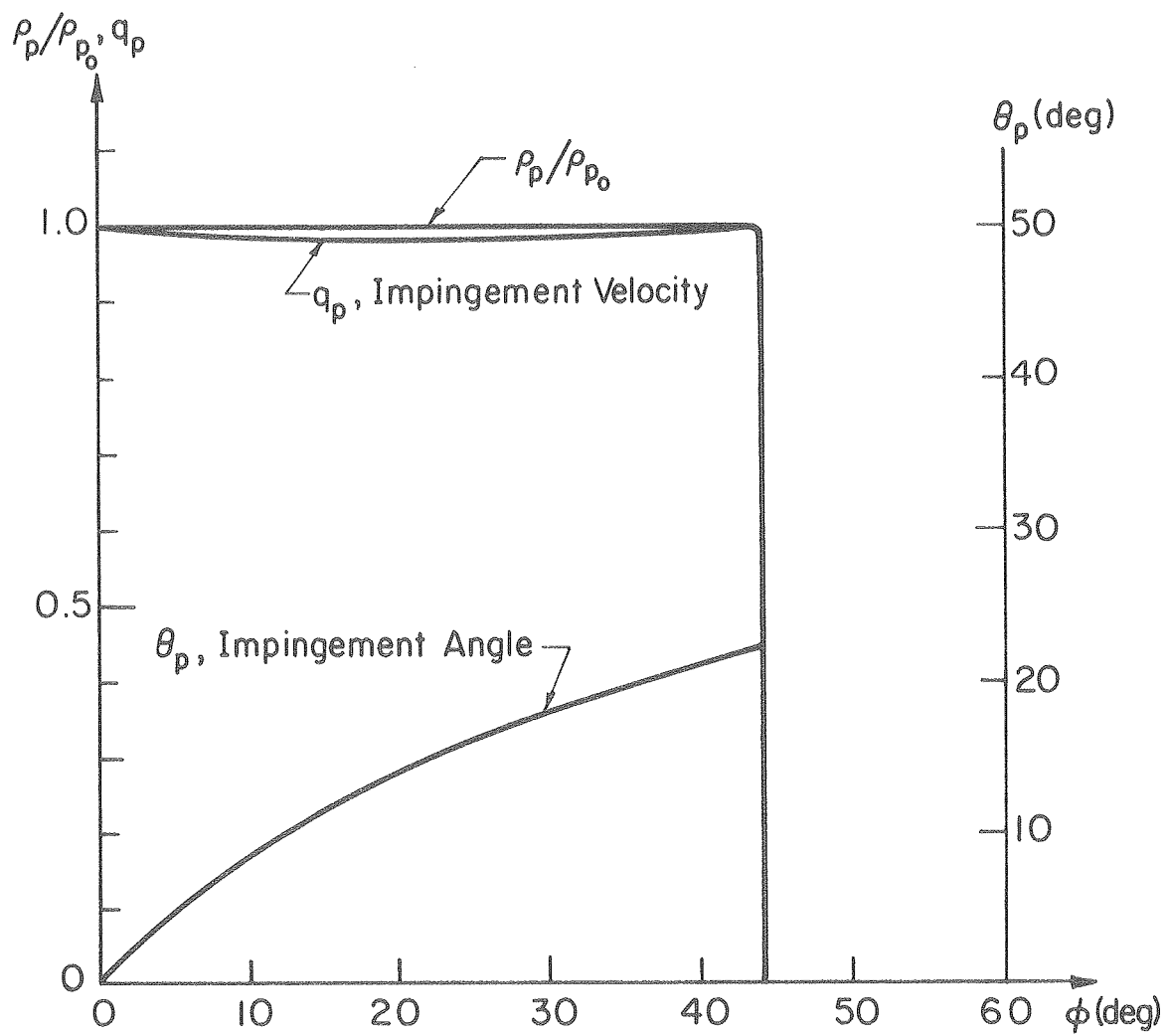
XBL 795-6223



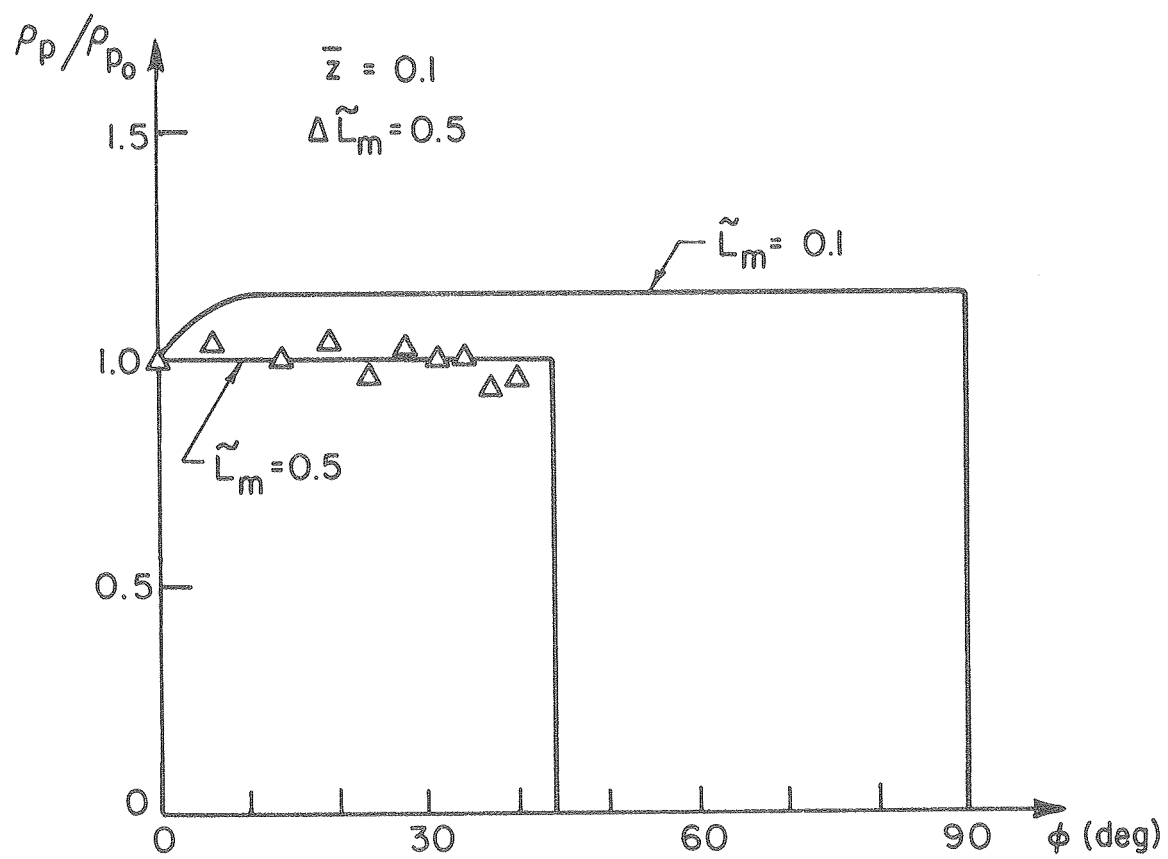
XBL795-6224



XBL 795-6225



XBL 795-6227



XBL795-6226

APPENDIXNote on the choice of ω , the relaxation constant

It has been mentioned that the outer edge velocity must be, in general, relaxed for the iteration between the core and the boundary layer regions to converge. The particular choice of ω depends very much on the individual problem. In the present case, the values of ω for convergence are relatively small. Consequently, a relatively large number of iterations need to be computed to acquire reasonable convergence results.

Various values of ω were used during the present analysis to determine the optimum value. For the first approximation ($N=1$), an optimum value of 0.01 has been found to yield converged results for the whole flow field after 35 iterations. The computation time is about 50 sec on a CDC 7600 machine. For the second approximation ($N=2$), the converged solution for the core region of the first approximation has been used to initiate the iteration process. As a result, comparatively large ω can be used, which in turn speeds up the convergence process. This is particularly crucial in the present analysis because the integration of the boundary layer equations for $N=2$ requires much more time than for the first approximation. Presently, ω is assigned a value of 0.1 and it takes about 40 iterations to obtain converged solution. The computation time is about 6 minutes, which is to be compared with 50 sec for the first approximation.

This report was done with support from the Department of Energy. Any conclusions or opinions expressed in this report represent solely those of the author(s) and not necessarily those of The Regents of the University of California, the Lawrence Berkeley Laboratory or the Department of Energy.

Reference to a company or product name does not imply approval or recommendation of the product by the University of California or the U.S. Department of Energy to the exclusion of others that may be suitable.

TECHNICAL INFORMATION DEPARTMENT
LAWRENCE BERKELEY LABORATORY
UNIVERSITY OF CALIFORNIA
BERKELEY, CALIFORNIA 94720